Electron Transport Layer Engineering Induced Carrier Dynamics Optimization for Efficient Cd-Free Sb(2) Se(3) Thin-Film Solar Cells

Ping Luo, Tahir Imran, Dong-Lou Ren, Jun Zhao, Ke-Wen Wu, Yu-Jia Zeng, Zheng-Hua Su, Ping Fan, Xianghua Zhang, Guang-Xing Liang, et al.

Electron Transport Layer Engineering Induced Carrier Dynamics Optimization for Efficient Cd-Free Sb_2Se_3 Thin-Film Solar Cells

*Ping Luo, Tahir Imran, Dong-Lou Ren, Jun Zhao, Ke-Wen Wu, Yu-Jia Zeng, Zheng-Hua Su, Ping Fan, Xiang-Hua Zhang, Guang-Xing Liang, and Shuo Chen**

P. Luo, T. Imaran, J. Zhao, K. Wu, Y. Zeng, Z. Su, P. Fan, G. Liang, S. Chen
Shenzhen Key Laboratory of Advanced Thin Films and Applications, Key Laboratory of Optoelectronic Devices and Systems of Ministry of Education and Guangdong Province, College of Physics and Optoelectronic Engineering
Shenzhen University
Shenzhen, Guangdong 518060, China
E-mail: chensh@szu.edu.cn (S. Chen)
D. Ren
State Key Laboratory of Featured Metal Materials and Life-cycle Safety for Composite Structures, MOE Key Laboratory of New Processing Technology for Nonferrous Metals and Materials, School of Resources, Environment and Materials
Guangxi University
Nanning, Guangxi 530004, China
X. Zhang
CNRS, ISCR (Institut des Sciences Chimiques de Rennes), UMR 6226
Université de Rennes
Rennes F-35000, France

Keywords: Sb_2Se_3; thin-film solar cells; Cd-free; electron transport layer; carrier dynamics

Abstract: Antimony selenide (Sb_2Se_3) is a highly promising photovoltaic material thanks to its outstanding optoelectronic properties, as well as its cost-effective and eco-friendly merits. However, toxic CdS is widely used as an electron transport layer (ETL) in efficient Sb_2Se_3 solar cells, which largely limit their development toward market commercialization. Herein, an effective green Cd-free ETL of SnO_x is introduced and deposited by atomic layer deposition method. Additionally, an important post-annealing treatment is designed to further optimize the functional

layers and the heterojunction interface properties. Such engineering strategy can optimize SnO_x ETL with higher nano-crystallinity, higher carrier density and less defect groups, modify Sb_2Se_3/SnO_x heterojunction with better interface performance and much desirable "spike-like" band alignment, and also improve the Sb_2Se_3 light absorber layer quality with passivated bulk defects and prolonged carrier lifetime, and therefore to enhance carrier separation and transport while suppressing non-radiative recombination. Finally, the as-fabricated Cd-free $Mo/Sb_2Se_3/SnO_x/ITO/Ag$ thin-film solar cell exhibits a stimulating efficiency of 7.39%, contributing a record value for Cd-free substrate structured Sb_2Se_3 solar cells reported to date. This work provides a viable strategy for developing and broadening practical applications of environmental-friendly Sb_2Se_3 photovoltaic devices.

1. Introduction

With the increasing demand for energy conversion applications, photovoltaic technology, which enables the direct conversion of renewable solar energy into environmental-friendly electrical power, is a vital technology under hotspot. Among diverse types of solar cells, cadmium telluride (CdTe)[1], copper indium gallium selenide (CIGS)[2], and gallium arsenide (GaAs)[3] solar cells have achieved great commercial success. However, the poisonous nature of cadmium (Cd), and the scarcity nature of indium (In), tellurium (Te), and gallium (Ga) are non-negligible limitation concerns. In the last decade, reserve-rich and environmentally sustainable antimony selenide (Sb_2Se_3) has become a very competitive contender as light absorbing photovoltaic material. This can be attributed to its exceptional optoelectronic attributes, such as an appropriate

bandgap (1.1-1.3 eV, matching well with the optimal Shockey-Queisser value), high absorption coefficient ($>10^5$ cm^{-1}), and superior carrier mobility (~15 cm^2 V^{-1}).[4-7]

The reported laboratory-scale power conversion efficiency (PCE) for Sb_2Se_3 solar cells has exceeded 10%[8,9], but most of the current devices are using cadmium sulfide (CdS) as the electron transport layer (ETL) or named as buffer layer. The CdS-based ETL brings three additional problems: First, its composition contains the toxic element of Cd, which goes against the ideal green environmental demand. Second, its intrinsic bandgap is narrow (~2.4 eV), resulting in loss of device photocurrent caused by absorption of some high energy photons (e.g., wavelength of 400-600 nm). Third, the degradation of device efficiency caused by inevitable Cd cation and S anion kinetic diffusion under thermal and/or optical treatment.[10] To cope these issues, some wide bandgap Cd-free ETLs have been attempted to replace CdS in Sb_2Se_3 solar cells, such as SnO_2, TiO_2, ZnO, $Zn_{1-x}Sn_xO$, and $ZnO_{1-x}S_x$.[5,10-13] Among them, SnO_2 is considered highly advantageous for constructing heterojunction thin-film solar cell with Sb_2Se_3 owing to its exceptional characteristics including non-toxicity, appropriate bandgap, benign transparency and stability.[14] Besides, in theory, according to Drude-Smith mode, the carrier trapping process is more effectively suppressed in Sb_2Se_3/SnO_2 heterojunction compared to that in Sb_2Se_3/CdS heterojunction, and the stronger time-dependent backscattering coefficient for Sb_2Se_3/SnO_2 heterojunction indicates that it possesses much superior charge separation efficiency. Thus, the important charge extraction efficiency, which is contingent upon the balance between charge recombination and charge separation, would be faster by inference, further confirming the feasibility of SnO_2 as a suitable ETL in Sb_2Se_3 solar cells.[15]

Regarding experimental efforts, Tang's group first used spray pyrolysis processed SnO_2 as ETL in the planar heterojunction Sb_2Se_3 solar cells and obtained a PCE of 3.05% in 2017.[16] Subsequently, the La-doped SnO_2 with improved electrical conductivity and crystallinity was introduced and achieved a device PCE of 3.25%, as reported by Chen's group.[17] In parallel, TiO_2-modified SnO_2[18] and $CdCl_2$-treated SnO_2[19] prepared by spin-coating method were also investigated, the as-constructed Cd-free Sb_2Se_3 solar cells delivered progressive PCEs higher than 4%. However, it is still far inferior to that of CdS ETLs involved counterparts. The limitations in achieving high PCE of Sb_2Se_3/SnO_2 heterojunction solar cells can be attributed to several important factors, such as high resistivity of the intrinsic SnO_2 thin film, severe defects and defects-assisted non-radiative recombination at the heterojunction interface, and inadequate interfacial lattice matching and/or band alignment.[11,20,21] To overcome these challenges, effective SnO_2-based ETLs preparation techniques and suitable Sb_2Se_3/SnO_2 heterojunction interface engineering efforts are needed. Accordingly, first, atomic layer deposition (ALD) has emerged as a promising technique for preparing SnO_2 thin film with uniform, pinhole-free, and dense characters under a low deposition temperature, and recently, ALD processed SnO_2 has gained significant progress as an ETL in planar-type perovskite solar cells to achieve an impressive improvement in device efficiency.[22,23] Second, an interesting interface engineering strategy of Sb_2Se_3/CdS heterojunction annealing was reported by our group to obtain significant performance improvements in Sb_2Se_3 photovoltaic devices[4,24] and photoelectrochemical photocathodes[25], which can be attributed to the positive interface defects passivation and band alignment optimization. Thus, both these findings strongly trigger our sense to consider them in Sb_2Se_3/SnO_2 solar cells.

Herein, sputtered and selenized Sb_2Se_3 light absorber layer was first fulfilled, characterized by large compact grains and favorable [hk1] growth orientation. Then, ALD processed SnO_x thin layer was introduced as ETL to construct Cd-free substrate structured Mo/Sb_2Se_3/SnO_x/ITO/Ag thin-film solar cells. Importantly, an additional vacuum post-annealing has been discovered to substantially enhance the device efficiency, thanks to the modified microstructure and optoelectronic properties of the SnO_x ETL, the suppressed defects at both interface and bulk regions, and the optimized carrier dynamics under band alignment tailoring. As a result, an interesting PCE of 7.39% can be achieved, representing the record value for Cd-free substrate structured Sb_2Se_3 solar cells. This work demonstrates a versatile strategy for enhancing environmental-friendly Sb_2Se_3 photovoltaic devices performance, as well as broadening their range of potential applications.

2. Results and Discussion

Herein, ALD processed SnO_x was sued as ETL to fabricate Cd-free substrate structured Sb_2Se_3 thin-film solar cells under configuration of Mo/Sb_2Se_3/SnO_x/ITO/Ag. To obtain the most suitable SnO_x ETL, a systematic investigation of its deposition process and post-treatment has been carried out. To be specific, the ALD deposition temperature-dependent and post-annealing temperature-dependent photovoltaic performance evolution of the Sb_2Se_3 solar cells are shown in Figure S1 and Figure S2 (Supporting Information), respectively. Accordingly, the optimal ALD deposition temperature for SnO_x is 105 °C, which is available to obtain smooth and dense SnO_x ETL (Figure S3a). In parallel, as shown in **Figure 1**a1-a4, the statistical distributions of the crucial photovoltaic performance parameters, an additional ETL or defined as heterojunction post-

annealing treatment under appropriate temperature (i.e., 250 °C) demonstrates a strong and credible positive effect on the performance, that deserves more detailed analysis. Current density-voltage (*J*-*V*) curves of the representative Sb_2Se_3/SnO_x thin-film solar cell without post-annealing (denoted as W/O annealing) and the champion annealed counterpart (denoted as With annealing) are shown in Figure 1b. Furthermore, Table 1 lists the corresponding photovoltaic parameters for thorough evaluation and analysis. The W/O annealing device presents a short-circuit current density (J_{SC}) of 23.22 mA cm^{-2}, open-circuit voltage (V_{OC}) of 0.370 V, fill factor (FF) of 53.99%, and therefore a PCE of 4.64% under the simulated AM 1.5 G solar irradiation. By contrast, the With annealing demonstrates a substantial enhancement of PCE to 7.39%, accompanied by synchronously enhanced J_{SC} (29.34 mA cm^{-2}), V_{OC} (0.407 V), and FF (61.96%). For further comparison, we summarize the PCEs of previously reported Cd-free Sb_2Se_3 solar cells according to the literatures (Figure 1c and Table S1).[5,10,12] It is worth mention that the PCE of 7.39% obtained in this work is slightly inferior to the highest value of 8.03% belonging to champion $FTO/TiO_2/Sb_2Se_3$/Spiro-OMeTAD/Au superstrate thin-film solar cell, representing the record value for substrate structured Cd-free Sb_2Se_3 solar cells reported to date.[10]

Figure 1d displays the spectra of external quantum efficiency (EQE) for both of these devices. The device subjected to annealing treatment exhibits a satisfied and broadband EQE spectra with peak value approaching 100%. This value is significantly higher than that of Sb_2Se_3 solar cells with the best performance based on CdS ETL. Moreover, using wide-bandgap SnO_x as ETL can greatly improve the EQE in the short wavelength (300-500 nm) in comparison to the corresponding cell

using CdS as ETL, which is closely related to the low absorption coefficient of SnO_x, especially for high energy photons. In addition, the With annealing device possesses a higher photoresponse than the W/O counterpart over the major spectral region (i.e., 400-1000 nm), indicating a reduction in non-radiative recombination losses within the space charge region (SCR). The integrated J_{SC} calculated from EQE spectra are found to be in good agreement with the corresponding *J-V* measurement determined J_{SC} values, and confirming more excellent carrier collection efficiency for the annealed device.[26] The Urbach energy (E_U) serves as an indicator to quantify the magnitude of the band tail effect and is typically determined from the ln(−ln(1−EQE)) versus Energy curve, as illustrated in Figure 1e. After post-annealing treatment, a significative drop in E_U from 27 to 21 meV becomes apparent, hinting that the recombination near the Sb_2Se_3/SnO_x heterojunction region might be suppressed thanks to the detrimental defects passivation, which will be unveiled later.

To investigate the morphology and microstructure of the Sb_2Se_3/SnO_x heterojunction, transmission electron microscopy (TEM) analysis was conducted on the With annealing device. **Figure 2**a displays a cross-sectional TEM image of the device, revealing a distinct layered structure consisting of a Sb_2Se_3 absorber layer, a SnO_x ETL, and an ITO window layer, with approximate thicknesses of 1500 nm, 30 nm, and 400 nm, respectively, which largely matches its SEM analysis (Figure S4a). High-angle annular dark field scanning-transmission electron microscopy (HAADF-STEM) was employed to examine the heterojunction interface characters between Sb_2Se_3 and SnO_x, as shown in Figure 2b. The observation indicates a well-defined high-quality heterojunction interface without

any observable distortion, dislocation, or amorphous layer.[27] Additionally, the SnO_x ETL shows nanocrystalline nature, and can be confirmed by its ring-shaped selected area electron diffraction (SAED) pattern with a typical polycrystalline structure (Figure 2c). Actually, SnO_x thin films prepared by ALD are typically amorphous as reported in some literatures, suggesting that the additional post-annealing process facilitates the transformation of SnO_x from an amorphous state to a nanocrystalline state.[28-30] Furthermore, atomic force microscopy (AFM) analysis illustrates that the as-annealed SnO_x sample demonstrates reduced surface roughness in comparison to the untreated counterpart (Figure S3). According to some relevant studies, this more smooth and dense nanocrystalline ETL would enhance the electron carrier extraction/transport efficiency, effectively mitigating carrier recombination and minimizing current leakage at the heterojunction interface.[29,31] Figure 2d shows a representative Gaussian blur processed HAADF-STEM image corresponds to Figure 2d exhibits a representative HAADF-STEM image that has undergone Gaussian blur processing. This image corresponds to a specific region within the intermediate area of the Sb_2Se_3 absorber layer. The distinct lattice fringes exhibiting spacings of 0.316 nm and 0.287 nm correspond remarkably well to the (211) and (221) lattice planes of Sb_2Se_3, respectively. Notably, periodic spots can be connected to the orthorhombic phase Sb_2Se_3, presenting obvious arrangement of $(Sb_4Se_6)_n$ nanoribbons in parallel along the [001] direction.[32] As shown in the SAED pattern (Figure 2e), the significantly higher diffraction intensities of the (221), (211), and (002) planes further demonstrate its [hk1] preferential growth orientation, which are also in agreement with the X-ray diffraction (XRD) results (Figure S5). Based on the previous theoretical and experimental findings, it can mitigate recombination losses

occurring at grain boundaries, facilitate carrier transport across the entire absorber layer, consequently leading to notable improvements in device performance.[4,6] Finally, Figure 2f and g depict the elemental composition distribution across the device's cross-section obtained through energy-dispersive X-ray spectroscopy (EDS) examination. Its corresponding elements exhibit a reasonable distribution, with epitaxial presentation of tin (Sn) and oxygen (O) elements between Sb_2Se_3 and ITO. The absence of element interdiffusion also indicates high structure stability to reduce the risk of device performance attenuation. Overall, the TEM characterization validates the excellent quality of the SnO_x ETL, Sb_2Se_3 absorber layer, as well as its engineered heterojunction interface, providing compelling evidence to construct an efficient Cd-free thin-film solar cell.

To observe the topography and surface potential distribution of Sb_2Se_3/SnO_x thin-film samples, comprehensive characterizations were conducted using Kelvin probe force microscopy (KPFM). The AFM micrographs in **Figure 3a** and e depict the surface morphologies of the W/O annealing and With annealing Sb_2Se_3/SnO_x samples, while their surface potential distributions are shown in Figure 3b and f, respectively. The AFM images reveal well-defined crystal grains and a smooth surface devoid of any pinholes, which is consistent with the top-view SEM image of the Sb_2Se_3 thin film (Figure S4b). The surface potential mappings were derived by aligning the linear markers within the topography (Figure 3c and g), and the corresponding schematic band bending diagrams are presented in Figure 3d and h. Notably, in both samples, the contact potential difference (V_{CPD}) at the grain boundaries (GBs) is higher than that at the grain interiors (GIs), indicating the Fermi energy level of GBs is closer to the vacuum level, resulting in a downward band bending at the GBs, which facilitates the spatial separation of holes and

electrons.[33] Further comparing the un-annealed sample to the annealed sample, the V_{CPD} value between the GBs and GIs is significantly reduced from 10 mV to 2 mV, indicating a lesser degree and more appropriate band bending at the GBs in the annealed sample.[6,34] Such benign band bending helps prevent electron trapping by defects at the GBs, thereby promoting charge carrier transport and collection while suppressing carrier recombination.

To further investigate the important influence of post-annealing treatment, X-ray photoelectron spectroscopy (XPS) and ultraviolet photoelectron spectroscopy (UPS) were employed on Sb_2Se_3/SnO_x thin films without and with annealing treatment. First, the XPS analysis was peak-fitted using a Gaussian-Lorentzian function after subtracting the Shirley background. XPS spectra of the Sn 3d core level regions on the film surfaces are deconvoluted for both samples (**Figure 4**a-b). The spectroscopy calculation reveals that the Sn/O ratio for the *in-situ* ALD processed SnO_x film is close to 2, in agreement with previously reported work.[29] In comparison, the ratio of Sn/O for the SnO_x sample with post-annealing treatment drops to 1.90. Regarding the same sensitivity factor, the latter sample contains two distinct valence states of Sn ions, i.e., Sn^{4+} and Sn^{2+}. The original XPS spectra and the corresponding fitted curves of the O 1s peaks for the without and with annealing samples are shown in Figure 4c and d, respectively. Each O 1s peak may be decomposed in four distinctive peaks, with the binding energy of 530.6 eV corresponding to Sn^{4+} atoms and the binding energy of 529.8 eV associated with Sn^{2+} atoms. The peak intensity ratio between these peaks provides further support for the aforementioned analysis of the Sn 3d spectra. Moreover, the presence of oxygen vacancies (i.e., V_O) is indicated by a peak at 531.7 eV, whereas the peak observed at 532.9 eV can be attributed to the existence of hydroxide (e.g., -OH

groups).[35] The percentage of area corresponding to each peak are listed in Table S2. Typically, the -OH group originated from the ALD process forms a trap state at the surface and/or interface, and its attenuated peak intensity underwent post-annealing indicates an effective passivation. Further comparison, the V_O determined peak intensity in the annealed sample is remarkably higher, suggesting that an additional post-annealing can increase the content of oxygen vacancies in the SnO_x ETL. These oxygen vacancies might act as negative electron acceptors and exhibit a strong electron attraction to Sn atoms, causing the Sn 3d peak to shift towards higher binding energy (Figure 4a and b).[35] Moreover, introducing oxygen vacancies appropriately, as illustrated in related studies, can enhance the electrical conductivity and carrier density of the SnO_x layer,[35] thereby facilitating charge carrier transport. In parallel, UPS tests were conducted to sightsee the band structure evolution. As shown in Figure 4e and f, the binding energy value of the secondary electron cut-off (E_{cutoff}) edge of the SnO_x thin film with and without post-annealing is 17.30 and 17.37 eV, respectively. The energy gap (E_{onset}), denoting the difference between the valence band maximum (VBM) and Fermi energy (E_F), can be obtained by linearly extrapolating of the leading edge of the UPS spectra (inset in Figure 4c and d), yielding values of 3.57 and 3.20 eV, respectively. Thus, substituting the E_{cutoff} and E_{onset} values into the following equations allow the determination of the position of conduction band (E_C), valence band (E_V) and Fermi levels (E_F):[6]

$$\begin{cases} \varphi = hv - E_{\text{cutoff}} \\ E_{\text{v}} = -\varphi - E_{\text{onset}} \\ E_{\text{c}} = E_{\text{v}} + E_{\text{g}} \end{cases} \quad (1)$$

where φ represents the work function (i.e., the absolute value of E_F assuming 0 eV for vacuum level), hv is the UV photoelectron energy of 21.22 eV, and E_g represents the bandgap value that can be calculated from the transmittance spectra (Figure S6 and Supplementary Note S1). Thus, E_C and E_V of the W/O annealing SnO_x are calculated as −3.45 and −7.42 eV, whereas presents an observable up-shift to −3.19 and −7.12 eV for With annealing sample. According to the literature[36], the bandgap and band structure changes of SnO_x is closely related to the increase of oxygen vacancies after post-annealing, which will widen the defective band, and in turn reduce the gap between the conduction band and the defective band. In addition, to further evaluate its modification, Mott-Schottky (*M-S*) measurements were conducted as described in Figure S7 and Supplementary Note S2, both non-annealed and annealed SnO_x exhibit typical n-type behaviors, the flat band potential (E_{fb}) coupled E_V value shows a synchronous up-shift, the carrier density (N_D) increases from 3.72×10^{17} cm^{-3} to 3.96×10^{18} cm^{-3}, achieving an order of magnitude enhancement after post-annealing treatment, consistent with the aforementioned XPS and UPS analysis. Finally, the schematic diagrams of band alignment for Sb_2Se_3/SnO_x (W/O annealing) and Sb_2Se_3/SnO_x (With annealing) heterojunction are depicted in Figure 4g and h, respectively, wherein, energy band position of the Sb_2Se_3 absorber layer is considered unchanged and determined through its reflectance spectrum and UPS spectrum (Figure S8, Supplementary Note S3). The conduction band offsets (CBO) of the Sb_2Se_3/SnO_x heterojunctions without and with annealing are determined to be −0.13 eV and 0.13 eV, as examined by a typical electron affinity (χ) model.[37] Thus, a "cliff-like" band alignment at the Sb_2Se_3/SnO_x (W/O annealing) heterojunction indicates a blocked electron injection under forward bias, resulting in a sharp reduction in carrier

lifetimes at the interface, and therefore a substantial loss in V_{OC} of the solar cell.[38] In contrast, a "spike-like" CBO is observed in the annealed Sb_2Se_3/SnO_x heterojunction. Furthermore, the obtained positive CBO value falls within the optimal value range (0-0.4 eV) for high-performance semiconductor heterojunction, which is really beneficial to suppressing the defects-involved recombination, promoting the carrier separation and transport efficiencies, and ultimately improving device efficiency.[38]

In general, improvements in photovoltaic performance are closely related to the enhanced heterojunction quality, particularly with regards to reduce carrier recombination at heterojunction interface. To assess the recombination process in these devices and further elucidate the working mechanism of Sb_2Se_3/SnO_x heterojunction annealing for optimizing device PCE, the following characterizations were conducted. The dark *J*-*V* curves (Figure S9) of both devices exhibit distinct rectification characteristics under a bias voltage range spanning from −1 V to 1 V. Subsequently, the shunt conductance (*G*), series resistance (*R*), diode ideality factor (*A*), and reverse saturation current density (J_0) parameters are derived through the following equation:[27]

$$J = J_0 \times exp\left[\frac{q}{AkT}(V - RJ)\right] + GV - J_L \quad (2)$$

Figure 5a presents plots of d*J*/d*V* against *V*, revealing flat regions fitted *G* values of the devices without and with annealing are respectively determined to be 0.122 and 0.006 mS/cm^2. The plots of d*V*/d*J* versus $(J+J_{SC})^{-1}$ in Figure 5b are employed for the determination of *R* and *A* through the fitting of the y-axis intercept and slope of the flat region. The W/O annealing device exhibits an *R* value of 6.56 Ω·cm^2, which decreases to 3.44 Ω·cm^2 in the With annealing device. Importantly,

the W/O annealing device possesses an obvious larger A value of 2.12 as compared to 1.43 for the annealed counterpart, indicating the presence of severe interface and SCR recombination in the former device, and a successful suppression of carrier recombination losses through heterojunction annealing treatment.[4] As shown in Figure 5c, the $\ln(J+J_{SC}-GV)$ versus $V-RJ$ plots reveal a synchronous decrease in the J_0 values from 7.6×10^{-3} to 4.5×10^{-4} mA·cm^{-2}, demonstrating the suppression of shunt path and enhancement of carrier transport. Figure 5d display the logarithmic dark J-V curves of these two devices, from which the defect density (N_{trap}) can be determined as follows:[39]

$$N_{trap} = \frac{2\varepsilon\varepsilon_0 V_{TFL}}{qL^2} \quad (3)$$

where L represents the thickness of Sb_2Se_3 thin film, ε signifies the relative dielectric constant (i.e., 15.1 for Sb_2Se_3), ε_0 denotes the vacuum dielectric constant, q is the elementary charge, and TFL voltage (V_{TFL}) is defined as the cross point of the trap filled limit (TFL) region (indicated by the blue rectangle region) and ohmic region (indicated by the green rectangle region).[39] The values of V_{TFL} for the W/O annealing and With annealing devices are respectively determined to be 0.21 V and 0.17 V. Consequently, the obtained N_{trap} value for the annealed device exhibits a slight decrease from 1.72×10^{15} cm^{-3} to 1.39×10^{15} cm^{-3}, confirming a reduction in the number of trap sites and defect recombination centers. Furthermore, temperature-dependent V_{OC} (V_{OC}-T) analysis was conducted to explore the recombination mechanisms regarding where and how the recombination occurred. The activation energy (E_a) can be determined by intercepting the y-axis in the graphs (Figure 5e). In general, thin-film solar cells exhibit two common recombination mechanisms, i.e., interface recombination-dominated mechanism

(E_a < E_g) and SCR recombination-dominated mechanism (E_a = E_g).[27] The values of E_a are noticeably lower than their respective bandgap values, indicating that interface recombination predominantly contributes to the performance losses in photovoltaics.[39] However, the heterojunction annealing treatment has positively alleviated interface recombination. To validate it, measurements of capacitance-voltage (*C-V*) and drive-level capacitance profiling (DLCP) were performed (Figure 5g). The built-in voltage (V_{bi}), which signifies the maximum open-circuit voltage (V_{OC}) value under illumination, is determined by intercepting the x-axis of the C^{-2}-*V* plots (Figure 5f). [37] The values of V_{bi} are found to be 0.483 V for the non-annealed device and 0.558 V for the annealed device, echoing higher heterojunction quality and V_{OC} in the latter scenario. Additionally, V_{bi} can also be determined using the following equation:[40]

$$V_{bi} = \frac{k_B T}{q} ln\left(\frac{N_A N_D}{{n_i}^2}\right) \quad (4)$$

where k_B represents the Boltzmann constant, T denotes the temperature, n_i is the intrinsic carrier concentration, and N_A and N_D correspond to the acceptor density and donor density in the Sb_2Se_3 and SnO_x, respectively. Thus, the value of V_{bi} demonstrates a direct proportionality to the logarithm of the carrier density, and the increase in V_{bi} can be attributed to the enhanced N_D in the SnO_x ETL after post-annealing treatment, as supported by the previous *M-S* analysis (Figure S7). The doping density in *C-V* measurements ($N_{C\text{-}V}$) is more sensitive to interfacial defect density (N_i) compared to the doping density measured by DLCP (N_{DLCP}).[6] As shown in Figure 5g, the discrepancy between N_{DLCP} and N_{CV} (equals to N_i value) of the unannealed device is significantly higher than that of the annealed counterpart, presenting as-estimated N_i values of 4.45×10^{16} cm^{-3} and 2.66×10^{15}

cm^{-3} at zero bias, respectively, confirming the suppression of both interface defects and defects-assisted recombination in the annealed device. Furthermore, the annealed device exhibits a significantly larger depletion width (W_d of 214 nm, corresponds to the profile depth value at v=0 V), indicating a fully-depleted SnO_x ETL and partially-depleted Sb_2Se_3 absorber layer. Such a result is expected considering the correlation between W_d and V_{bi}, and it is among the most satisfied values for efficient chalcogenide thin-film photovoltaic devices with beneficial light absorption and carrier extraction.[32] Transient photovoltage (TPV) analysis is utilized as a powerful technique to explore and elucidate the intricate dynamics of carrier recombination in the devices. Owing to the absence of hysteresis effect, the TPV spectra are analyzed by fitting decay curves with a simple mono-exponential model, from which the recombination lifetime can be obtained.[41] As illustrated in Figure 5h, the photovoltage decay lifetime (τ_{TPV}) of the annealed device is leaped from 4 to 244 μs, indicating a significant reduction in carrier recombination.[42] Electrochemical impedance spectroscopy (EIS) analysis was subsequently employed to delve into the detailed charge carrier recombination and transfer characteristics. Figure 5i shows the Nyquist plots of both devices, with an inset depicting a representative equivalent circuit model. The recombination resistances (R_{rec}) of the devices are determined by the diameter length of the fitted arc as 2578 and 82055 Ω, authenticating the reduced likelihood of charge recombination at the heterojunction interface in the annealed device. In addition, the charge transport resistance (R_{tra}) is ascertained by intercepting the x-axis, yielding values of 25.98 and 12.74 Ω for un-annealed and annealed devices, respectively. A lower R_{tra} value reflects improved carrier transport efficiency, which justifies the higher J_{SC} and PCE observed in device subjected to

heterojunction post-annealing treatment. Thanks to this engineering effort, a significantly enhanced heterojunction is achieved, characterized by improved diode ideality factor, built-in voltage, depletion width, photovoltage decay lifetime, and a more favorable interface with reduced defect density, as summarized in Table 2. These advancements contribute to the enhancement of charge carrier generation, separation and transport, leading to improved photovoltaic performance in Cd-free Sb_2Se_3/SnO_x solar cells.

Admittance spectroscopy was employed to gain insights into the bulk defect properties, especially assess the impact of heterojunction annealing treatment on defects distribution inside the device. Temperature-dependent capacitance-frequency (*C-f-T*) analysis was conducted on the un-annealed (**Figure 6a**) and the annealed devices (Figure 6d), covering a measurement temperature range from 110 to 300 K with 10 K increments, and frequencies ranging from 10^2 Hz to 10^6 Hz. The defect emission frequency (ω_0) was determined by identifying the angular frequency point ω at which the maximum value of the plot for $\omega dC/d\omega$ was observed. The defect activation energies (E_A) were calculated using the Arrhenius formula as follows: [43]

$$\ln\left(\frac{\omega_0}{T^2}\right) = \ln(2v_0) - \frac{E_A}{k_B T} \quad (5)$$

where ν_0 denotes a constant proportional to attempt-to-escape frequency and effective Richardson constant, and k_B represents the Boltzmann constant. The E_A values of 396 meV and 385 meV were determined for the W/O annealing and With annealing devices, respectively, by calculating the slopes of the Arrhenius plots shown in Figure 6b and e. These E_A values are consistent with the previously reported experimental work and first-principle calculation results, where they are

commonly associated with selenium vacancy defects (V_{Se}) and antimony antisite defects (Sb_{Se}), known to act as recombination centers in the Sb_2Se_3-based photovoltaic devices.[4,39] To further obtain the defect density (N_T), a Gaussian fitting was applied using the Kimerling model:[43]

$$\begin{cases} E(\omega) = kT\ln\left(\frac{2\pi v_0 T^2}{\omega}\right) \\ N_T[E(\omega)] = -\frac{V_{bi}}{q\omega}\cdot\frac{dC}{d\omega}\cdot\frac{\omega}{kT} \end{cases} \quad (6)$$

where E represents the energetic distance between the defect energy level and the valence band maximum (VBM) or conduction band minimum (CBM). The bulk defect density spectra of the W/O annealing and With annealing devices are depicted in Figure 6c and f, respectively, indicating a significant decline in the N_T values from 1.87 × 10^{17} cm^{-3} to 3.27 × 10^{16} cm^{-3}. This variation signifies the effective passivation of bulk defects and non-radiative recombination within the light absorber layer. Combined with the aforementioned XPS analysis regarding the increased oxygen vacancies in the SnO_x ETL after annealing treatment, thus, appropriate oxygen diffusion from SnO_x might form ultra-thin Sb_2O_3 at the interface, and even the diffusion of trace amounts of oxygen to bulk Sb_2Se_3 to further passivate the Se-related V_{Se} and/or Sb_{Se} detrimental defects.[44,45] Finally, the transient absorption spectroscopy (TAS) characterization was conducted on FTO/Sb_2Se_3/SnO_x samples to further sightsee the photo-generated bulk carrier dynamics upon the impact of post-annealing treatment. As illustrated in the 2D color images of TAS (Figure 6g and h), a distinct photo-induced absorption peak centered around 750 nm is observed in both samples, aligning with previous studies.[27] The kinetic curves at 750 nm were normalized and fitted using a typical biexponential decay kinetic model (Figure 6i):[4]

$$y = A_1 e^{-\frac{x}{\tau_1}} + A_2 e^{-\frac{x}{\tau_2}} \quad (7)$$

The short (τ_1) and long (τ_2) decay lifetimes along with their corresponding weighted coefficients (A_1 and A_2) are determined and summarized in Table S3. As shown in Table S3, both interface/surface recombination (corresponds to τ_1) and bulk recombination (corresponds to τ_2) have been suppressed. The average lifetime of the non-annealed sample is found to be 2317 ps, whereas for the annealed sample, it is 5818 ps. This strongly indicates the suppression of both recombination processes occurring at the interface/surface and within the bulk of the device following heterojunction annealing, echoing the above analysis of charge carrier dynamics and recombination mechanisms. Moreover, the obtained lifetime (τ of 5818 ps) is also comparable to those values in high-efficiency Sb_2Se_3 thin-film solar cells (Table S4).[4,8,46-49] Thus, the prolonged lifetime of photo-generated minority carriers ultimately contributes to an enhancement in the V_{OC} and PCE of the Cd-free Sb_2Se_3 photovoltaic devices.

3. Conclusions

In this work, ALD processed SnO_x has been introduced as an effective ETL to fabricate Cd-free substrate structured Sb_2Se_3 thin-film solar cell under configuration of Mo/Sb_2Se_3/SnO_x/ITO/Ag. After a systematic investigation of the key device performance, it has been found that the additional ETL post-annealing or functioned as heterojunction annealing treatment significantly enhances the overall device performance. It has illustrated that this important engineering effort could simultaneously improve SnO_x ETL quality with more smooth/dense nanocrystalline nature, less detrimental -OH groups and higher carrier density, improve the Sb_2Se_3/SnO_x heterojunction quality with better electrical properties,

less interface defects and much superior "spike-like" band alignment, and also improve the Sb_2Se_3 absorber layer quality through the passivation of bulk defects and extension of the carrier lifetime. Thus, the overall carrier recombination was suppressed, the carrier generation, separation and transport efficiencies were enhanced. Accordingly, the annealed solar cell delivers a competitive efficiency of 7.39%, representing the record value for Cd-free substrate structured Sb_2Se_3 thin-film solar cells. This work can pave the way for extensive investigations into the utilization of SnO_x or other eco-friendly semiconductors as ETLs in Cd-free thin-film photovoltaic devices, and the further improvement of device performance.

4. Experimental Section

Preparation of Sb_2Se_3 thin film: Ultrasonically cleaned Mo-coated soda lime glass was chosen as substrate. The fabrication process involved initial radio-frequency (RF) magnetron sputtering of the Sb precursor, followed by a controlled selenization heat treatment to facilitate the self-assembled growth of high-quality crystalline Sb_2Se_3 thin film for light absorption. The detailed preparation process can be found in our previous report [4,6,24].

Preparation of SnO_x ETL: The tin oxide (SnO_x) ETL was prepared onto the Sb_2Se_3 thin film using ALD method with tetrakis(dimethylamino)tin (TDMASn) and deionized water as the precursor sources for tin (Sn) and oxygen (O), respectively. The TDMASn precursor was stored in a temperature-controlled stainless steel vessel at a constant temperature of 65 °C, while the reaction chamber and the precursor delivery line were set to 105 °C. The specific parameters and ALD process flow are illustrated in Figure S10. Subsequently, a post-annealing treatment of the Sb_2Se_3/SnO_x samples was performed in a vacuum tubular furnace.

The chamber was heated to a temperature of 250 °C over a period of 10 minutes under vacuum condition and then maintained for 5 minutes.

Fabrication of Mo/Sb_2Se_3/SnO_x/ITO/Ag thin-film solar cells: Subsequent to the deposition of the Sb_2Se_3 absorber layer and SnO_x ETL, an indium tin oxide (ITO) window layer was fabricated via RF magnetron sputtering. The sputtering process parameters, including the applied power, working pressure, and duration, were set at 100 W, 0.35 Pa, and 25 minutes, respectively. The flow rates of argon (Ar) gas and oxygen (O_2) gas were adjusted at 30 sccm and 10 sccm, respectively. Finally, metallic contacts were established by thermal evaporation of silver (Ag) electrodes onto the surface. The active area of each solar cell device is 0.11 cm^2. A schematic illustration of the overall fabrication process for the substrate structured Mo/Sb_2Se_3/SnO_x/ITO/Ag thin-film solar cells is depicted in Figure S11.

Characterizations: The current density-voltage (*J-V*) characteristics of the thin-film solar cells were evaluated using a multimeter (Keithley, 2400 Series) under AM 1.5 G simulated sunlight illumination with intensity calibrated to 100 mW/cm^2. External quantum efficiency (EQE) spectra were obtained through a measurement system of Zolix SCS101 system. X-ray photoelectron spectroscopy (XPS) analysis was conducted using the PHI 5000 Versa Probe III instrument equipped with a monochromatic Al K_α X-ray source, and the spectra were calibrated based on the C 1s peak at 284.8 eV. Reflection spectra of Sb_2Se_3 absorber layer and transmittance spectra of SnO_x ETLs were acquired through a Shimadzu UV-3600 UV/Vis/NIR spectrophotometer. The band structure of the Sb_2Se_3 and SnO_x were then examined using ultraviolet photoelectron spectroscopy (UPS, PHI 5000 VersaProbe), employing a He I source of 21.22 eV. 2D/3D atomic force microscopy

(AFM) micrographs of the SnO_x ETLs were observed by a NT-MDT Spectrum Instrument under the semi-contact mode. Kelvin probe force microscopy (KPFM) characterizations were performing using a Dimension ICON system equipped with a gold-coated silicon cantilever to investigate both the topographies and surface potentials. The growth orientation information of Sb_2Se_3 thin film was investigated by X-ray diffraction (XRD, Ultima-iv diffractometer). Surface and cross-sectional morphologies of Sb_2Se_3 were obtained from scanning electron microscope (SEM, Zeiss SUPRA 55). Transmission electron microscope (TEM, FEI Titan Cubed Themis G2 300) was conducted to investigate the microstructure and morphology of the device, and a TEM-coupled energy dispersive spectroscopy (EDS) was attached to analyze the elemental distribution. Mott-Schottky (*M-S*) measurements were conducted using a CHI600E electrochemical workstation with an amplitude of 0.01 V and a frequency of 1 kHz. Electrochemical impedance spectroscopy (EIS) was obtained through electrochemical workstation, covering frequencies ranging from 1 Hz to 100 kHz. Capacitance-voltage (*C-V*) and Drive-level capacitance profiling (DLCP) measurements were performed on a Keithley 4200A-SCS system, employing an AC amplitude of 30 mV and frequency of 10 kHz, in conjunction with a JANIS cryogenic platform. Transient photovoltage (TPV) was performed using a 355 nm pulsed laser served as the light source, while the voltage signals were recorded using an oscilloscope (Tektronix TDS 3054C, 500 MHz). Temperature-dependent capacitance-frequency (*C-f-T*) measurements were carried out under a frequency range from 100 Hz to 100 kHz and a temperature range from 300 K to 110 K using Lakeshore 325 temperature controller. Transient absorption spectroscopy (TAS) analysis was conducted using a transient absorption spectrometer (Newport) equipped with a Spectra-Physics Solstice Ace regenerative

amplifier operating at a wavelength of 800 nm, generating 100 fs pulses at a repetition rate of 1 kHz.

Supporting Information

Supporting Information is available from the Wiley Online Library or from the author.

Acknowledgments

This work was supported by National Natural Science Foundation of China (No. 62104156, 62074102), Guangdong Basic and Applied Basic Research Foundation (2023A1515011256, 2022A1515010979) China, Science and Technology plan project of Shenzhen (20220808165025003, 20200812000347001) China. This project was also supported by open foundation of Guangxi Key Laboratory of Processing for Non-ferrous Metals and Featured Materials, State Key Laboratory of Featured Metal Materials and Life-cycle Safety for Composite Structures, Guangxi University (Grant No. 2022GXYSOF13).

Conflict of Interest

The authors declare no conflict of interest.

References

[1] D. B. Li, C. Yao, S. N. Vijayaraghavan, R. A. Awni, K. K. Subedi, R. J. Ellingson, L. Li, Y. Yan, F. Yan, *Nat. Energy*, **2021**, 6, 715-722.

[2] S. C. Yang, T. Y. Lin, M. Ochoa, H. Lai, R. Kothandaraman, F. Fu, A. N. Tiwari, R. Carron, *Nat. Energy*, **2023**, 8, 40-51.

[3] S. S. Lin, Z. Q. Wu, X. Q. Li, Y. J. Zhang, S. J. Zhang, P. Wang, R. Panneerselvam, J. F. Li, *Adv. Energy Mater.*, **2016**, 6, 1600822.

[4] R. Tang, S. Chen, Z. H. Zheng, Z. H. Su, J. T. Luo, P. Fan, X. H. Zhang, J. Tang, G. X. Liang, *Adv. Mater.*, **2022**, 34, 2109078.

[5] C. Chen, Y. Zhao, S. Lu, K. Li, Y. Li, B. Yang, W. Chen, L. Wang, D. Li, H. Deng, F. Yi, J. Tang, *Adv. Energy Mater.*, **2017**, 7, 1700866.

[6] Y. Luo, G. Chen, S. Chen, N. Ahmad, M. Azam, Z. Zheng, Z. Su, M. Cathelinaud, H. Ma, Z. Chen, P. Fan, X. Zhang, G. Liang, *Adv. Funct. Mater.*, **2023**, 33, 2213941.

[7] Y. Zhou, L. Wang, S. Chen, S. Qin, X. Liu, J. Chen, D. J. Xue, M. Luo, Y. Cao, Y. Cheng, E. H. Sargent, J. Tang, *Nat. Photonics*, **2015**, 9, 409-415.

[8] Y. Zhao, S. Wang, C. Li, B. Che, X. Chen, H. Chen, R. Tang, X. Wang, G. Chen, T. Wang, J. Gong, T. Chen, X. Xiao, J. Li, *Energy Environ. Sci.*, **2022**, 15, 5118-5128.

[9] Z. Duan, X. Liang, Y. Feng, H. Ma, B. Liang, Y. Wang, S. Luo, S. Wang, R. E. I. Schropp, Y. Mai, Z. Li, *Adv. Mater.*, **2022**, 34, 2202969.

[10] C. Liu, S. Wu, Y. Gao, Y. Feng, X. Wang, Y. Xie, J. Zheng, H. Zhu, Z. Li, R. E. I. Schropp, K. Shen, Y. Mai, *Adv. Funct. Mater.*, **2022**, 32, 2209601.

[11] J. Zhou, D. Meng, T. Yang, X. Zhang, Z. Tang, Y. Cao, J. Ni, J. Zhang, Z. Hu, J. Pang, *Appl. Surf. Sci.*, **2022**, 591, 153169.

[12] Y. D. Luo, M. D. Chen, R. Tang, M. Azam, S. Chen, Z. H. Zheng, Z. H. Su, P. Fan, H. L. Ma, G. X. Liang, X. H. Zhang, *Sol. Energy Mater. Sol. Cells*, **2022**, 240, 111721.

[13] I. Gharibshahian, A. A. Orouji, S. Sharbati, *Opt. Mater.*, **2021**, 116, 111098.

[14] C. Chen, K. Li, J. Tang, *Sol. RRL*, **2022**, 6, 2200094.

[15] Z. Zhang, M. Hu, T. Jia, J. Du, C. Chen, C. Wang, Z. Liu, T. Shi, J. Tang, Y. Leng, *ACS Energy Lett.*, **2021**, 6, 1740-1748.

[16] S. Lu, Y. Zhao, C. Chen, Y. Zhou, D. Li, K. Li, W. Chen, X. Wen, C. Wang, R. Kondrotas, N. Lowe, J. Tang, *Adv. Electron. Mater.*, **2018**, 4, 1700329.

[17] Z. Chen, H. Guo, C. Ma, X. Wang, X. Jia, N. Yuan, J. Ding, *Sol. Energy*, **2019**, 187, 404-410.

[18] X. Wang, H. Guo, C. Ma, X. Jia, Y. Li, N. Yuan, J. Ding, *Vacuum*, **2019**, 166, 201-205.

[19] J. Zhou, X. Zhang, H. Chen, Z. Tang, D. Meng, K. Chi, Y. Cai, G. Song, Y. Cao, Z. Hu, *Appl. Surf. Sci.*, **2020**, 534, 147632.

[20] Y. Wang, S. Ji, B. Shin, *J. Phys. Energy*, **2022**, 4, 044002.

[21] P. Wu, S. Wang, X. Li, F. Zhang, *J. Mater. Chem. A*, **2021**, 9, 19554-19588.

[22] T. Hu, T. Becker, N. Pourdavoud, J. Zhao, K. O. Brinkmann, R. Heiderhoff, T. Gahlmann, Z. Huang, S. Olthof, K. Meerholz, D. Többens, B. Cheng, Y. Chen, T. Riedl, *Adv. Mater.*, **2017**, 29, 1606656.

[23] B. Yu, F. Tang, Y. Yang, J. Huang, S. Wu, F. Lu, W. Duan, A. Lambertz, K. Ding, Y. Mai, *Adv. Mater.*, **2023**, 35, 2202447.

[24] G. X. Liang, Y. D. Luo, S. Chen, R. Tang, Z. H. Zheng, X. J. Li, X. S. Liu, Y. K. Liu, Y. F. Li, X. Y. Chen, Z. H. Su, X. H. Zhang, H. L. Ma, P. Fan, *Nano Energy*, **2020**, 73, 104806.

[25] G. Liang, T. Liu, M. Ishaq, Z. Chen, R. Tang, Z. Zheng, Z. Su, P. Fan, X. Zhang, S. Chen, *Chem. Eng. J.*, **2022**, 431, 133359.

[26] Z. Su, G. Liang, P. Fan, J. Luo, Z. Zheng, Z. Xie, W. Wang, S. Chen, J. Hu, Y. Wei, C. Yan,

J. Huang, X. Hao, F. Liu, *Adv. Mater.*, **2020**, 32, 2000121.

[27] G. Liang, M. Chen, M. Ishaq, X. Li, R. Tang, Z. Zheng, Z. Su, P. Fan, X. Zhang, S. Chen, *Adv. Sci.*, **2022**, 9, 2105142.

[28] J. H. Han, S. H. Lee, S. G. Jeong, D. Y. Kim, H. L. Yang, S. Lee, S. Y. Yoo, I. Park, H. B. Park, K. S. Lim, W. J. Yang, H. C. Choi, J.-S. Park, *ACS Appl. Mater. Interfaces*, **2021**, 13, 39584-39594.

[29] J. H. Lee, M. Yoo, D. Kang, H. M. Lee, W. h. Choi, J. W. Park, Y. Yi, H. Y. Kim, J. S. Park, *ACS Appl. Mater. Interfaces*, **2018**, 10, 33335-33342.

[30] J. Heo, A. S. Hock, R. G. Gordon, *Chem. Mater.*, **2010**, 22, 4964-4973.

[31] M. Januar, S. P. Prakoso, C. W. Zhong, H. C. Lin, C. Li, J. H. Hsieh, K. K. Liu, K. C. Liu, *ACS Appl. Mater. Interfaces*, **2022**, 14, 46726-46737.

[32] Y. D. Luo, R. Tang, S. Chen, J. G. Hu, Y. K. Liu, Y. F. Li, X. S. Liu, Z. H. Zheng, Z. H. Su, X. F. Ma, P. Fan, X.-H. Zhang, H. L. Ma, Z. G. Chen, G. X. Liang, *Chem. Eng. J.*, **2020**, 393, 124599.

[33] W. Yang, J. H. Kim, O. S. Hutter, L. J. Phillips, J. Tan, J. Park, H. Lee, J. D. Major, J. S. Lee, J. Moon, *Nat. Commun.*, **2020**, 11, 861.

[34] S. Chen, T. Liu, M. Chen, M. Ishaq, R. Tang, Z. Zheng, Z. Su, X. Li, X. Qiao, P. Fan, G. Liang, *Nano Energy*, **2022**, 99, 107417.

[35] X. Li, Z. Shi, F. Behrouznejad, M. Hatamvand, X. Zhang, Y. Wang, F. Liu, H. Wang, K. Liu, H. Dong, F. Mudasar, J. Wang, A. Yu, Y. Zhan, *J. Energy Chem.*, **2022**, 67, 1-7.

[36] F. Ali, N. D. Pham, H. J. Bradford, N. Khoshsirat, K. Ostrikov, J. M. Bell, H. Wang, T. Tesfamichael, *ChemSusChem*, **2018**, 11, 3096-3103.

[37] S. Chen, Y. Fu, M. Ishaq, C. Li, D. Ren, Z. Su, X. Qiao, P. Fan, G. Liang, J. Tang, *InfoMat*, **2023**, 5, e12400.

[38] K. Sun, C. Yan, F. Liu, J. Huang, F. Zhou, J. A. Stride, M. Green, X. Hao, *Adv. Energy Mater.*, **2016**, 6, 1600046.

[39] S. Chen, P. Luo, D. L. Ren, C. Y. Duan, X. F. Ma, Z. H. Su, Z. H. Zheng, P. Fan, G. X. Liang, R. Tang, *Appl. Surf. Sci.*, **2023**, 619, 156783.

[40] G. Liang, Z. Li, M. Ishaq, Z. Zheng, Z. Su, H. Ma, X. Zhang, P. Fan, S. Chen, *Adv. Energy Mater.*, **2023**, 13, 2300215.

[41] J. Shi, D. Li, Y. Luo, H. Wu, Q. Meng, *Rev. Sci. Instrum.*, **2016**, 87, 123107.

[42] J. Shi, Y. Li, Y. Li, D. Li, Y. Luo, H. Wu, Q. Meng, *Joule*, **2018**, 2, 879-901.

[43] P. Fan, G. J. Chen, S. Chen, Z. H. Zheng, M. Azam, N. Ahmad, Z. H. Su, G. X. Liang, X.

H. Zhang, Z. G. Chen, *ACS Appl. Mater. Interfaces*, **2021**, 13, 46671-46680.

[44] C. Wang, S. Lu, S. Li, S. Wang, X. Lin, J. Zhang, R. Kondrotas, K. Li, C. Chen, J. Tang, *Nano Energy*, **2020**, 71, 104577.

[45] N. Fleck, O. S. Hutter, L. J. Phillips, H. Shiel, T. D. C. Hobson, V. R. Dhanak, T. D. Veal, F. Jäckel, K. Durose, J. D. Major, *ACS Appl. Mater. Interfaces*, **2020**, 12, 52595-52602.

[46] Y. Wang, R. Tang, L. Huang, C. Qian, W. Lian, C. Zhu, T. Chen, *ACS Appl. Mater. Interfaces*, **2022**, 14, 33181-33190.

[47] X. Wen, C. Chen, S. Lu, K. Li, R. Kondrotas, Y. Zhao, W. Chen, L. Gao, C. Wang, J. Zhang, G. Niu, J. Tang, *Nat. Commun.*, **2018**, 9, 2179.

[48] R. Cao, H. Cai, W. Lian, R. Tang, Y. Xiang, Y. Wang, T. Chen, *J. Mater. Chem. A*, **2022**, 10, 20482-20488.

[49] H. Cai, R. Cao, J. Gao, C. Qian, B. Che, R. Tang, C. Zhu, T. Chen, *Adv. Funct. Mater.*, **2022**, 32, 2208243.

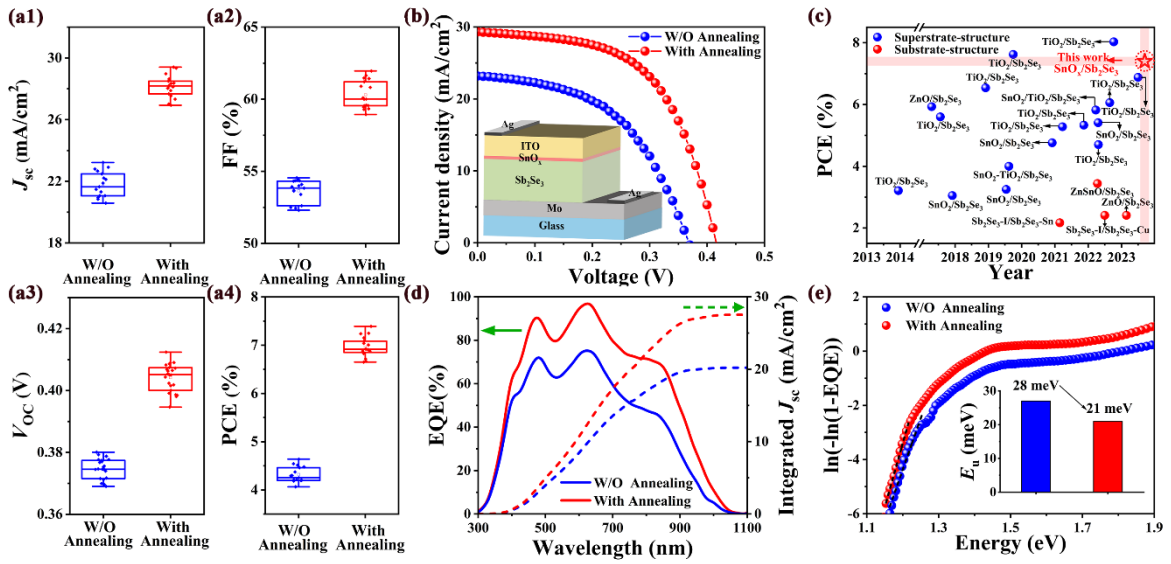

Figure 1. Statistical distribution and characterization of key performance parameters of the W/O annealing and With annealing Sb_2Se_3/SnO_x thin-film solar cells, including (a1) J_{SC}, (a2) FF, (a3) V_{OC}, and (a4) PCE. (b) *J-V* curves of the representative W/O annealing and With annealing Sb_2Se_3/SnO_x thin-film solar cells. (c) Comparative analysis of this study with state-of-the-art Cd-free Sb_2Se_3 thin-film solar cells. (d) EQE and integrated J_{SC} of the representative devices. (e) The Urbach energy values obtained from EQE spectra.

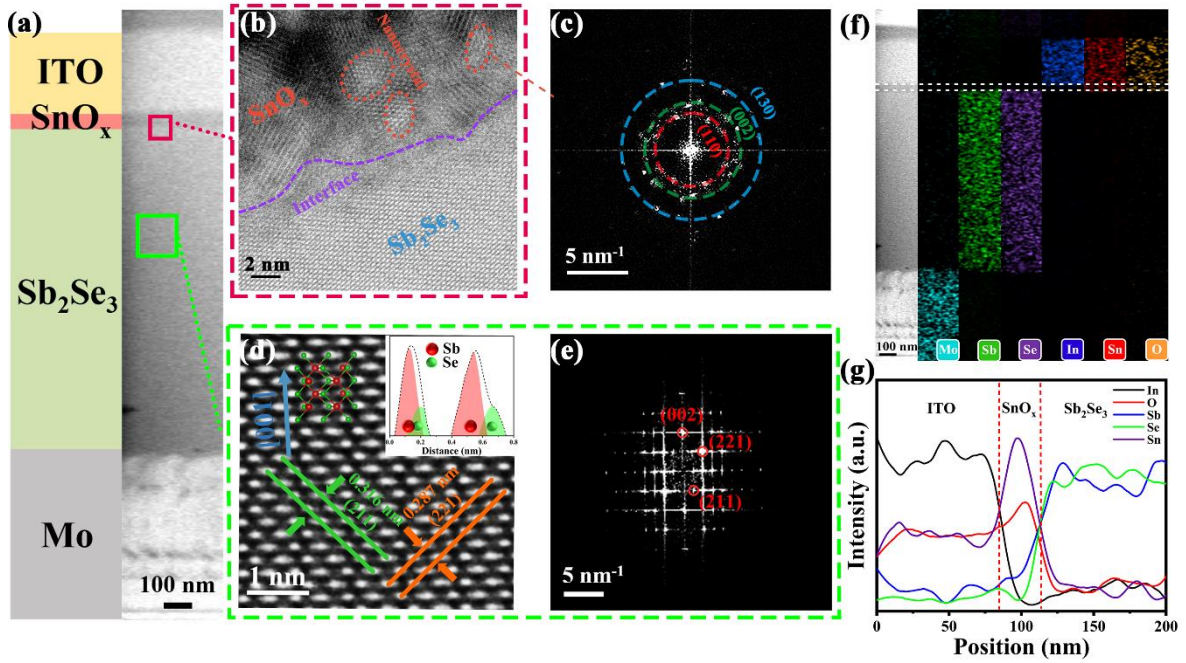

Figure 2. TEM characterization of the champion With annealing Sb_2Se_3/SnO_x device. (a) Cross-sectional TEM image. (b) HAADF-STEM image showing the Sb_2Se_3/SnO_x heterojunction interface. (c) SAED pattern corresponds to the SnO_x ETL region. (d) Gaussian-blurred HAADF-STEM image of the bulk Sb_2Se_3 absorber layer region, inset of an intensity profile of Sb and Se atoms, and an [001]-oriented $(Sb_4Se_6)_n$ ribbon. (e) The corresponding SEAD pattern of Sb_2Se_3. (f) EDS elemental mappings, and (g) EDS elemental line scan profiles across the Sb_2Se_3/SnO_x/ITO sections of the device.

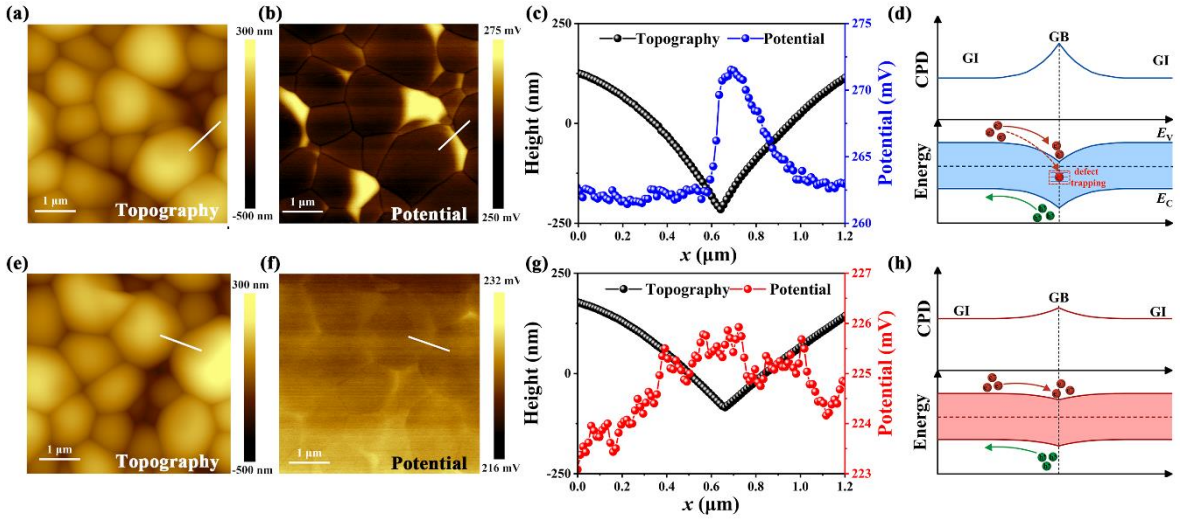

Figure 3. KPFM analysis of the representative W/O annealing (a-d), and With annealing (e-h) Sb_2Se_3/SnO_x samples. (a) Topography, (b) CPD mapping, (c) topography and potential line scans, and (d) schematic band bending diagram. (e-h) The corresponding KPFM results of the annealed sample.

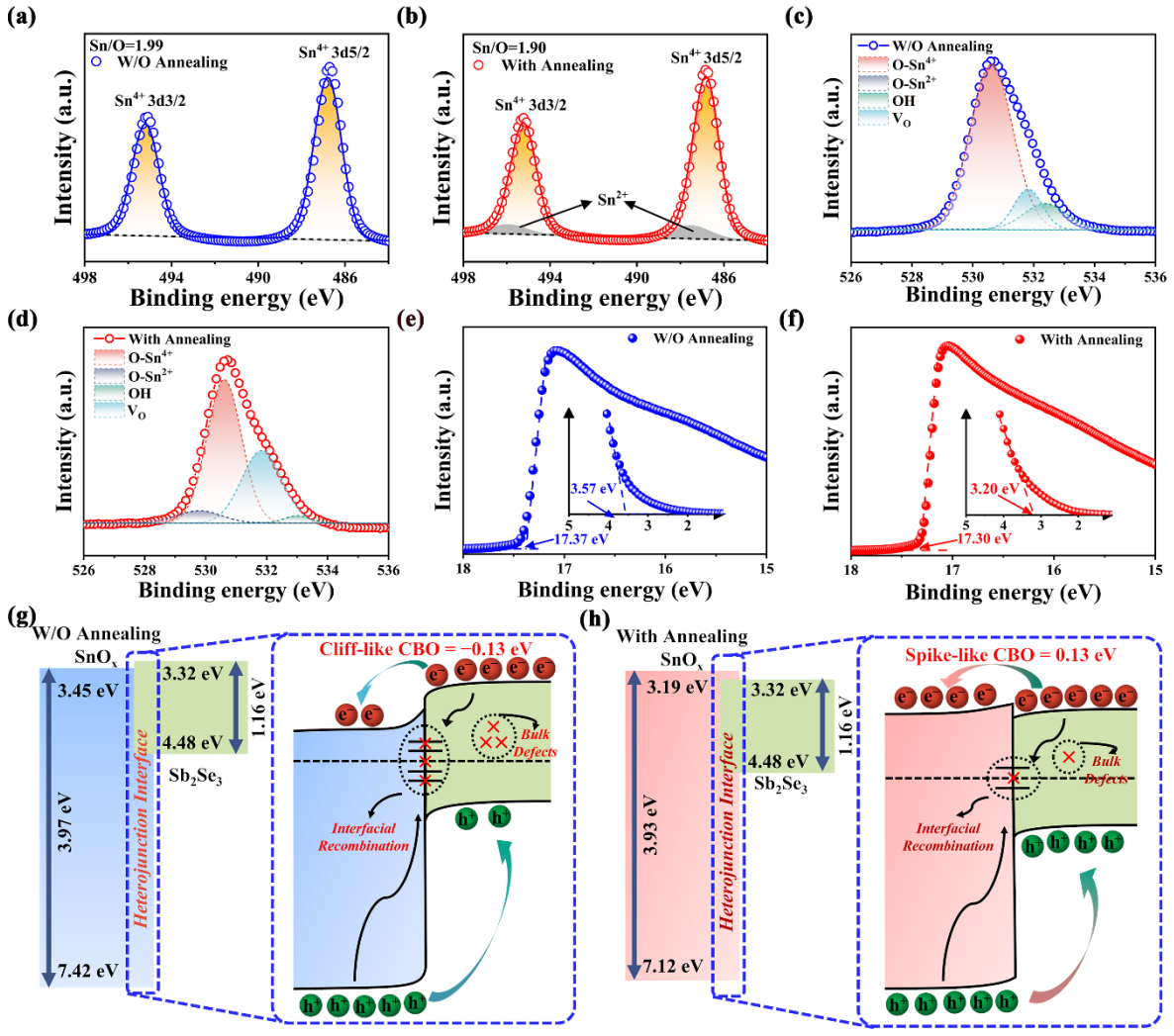

Figure 4. (a, b) Sn 3d XPS spectra of (a) the W/O annealing and (b) With annealing Sb_2Se_3/SnO_x thin films. (c, d) The corresponding O 1s XPS spectra, and (e, f) UPS characterizations, used to derive SEC edge and VB position. (g-h) The schematic band alignment of (g) W/O annealing and (h) With annealing heterojunctions, accompanied with illustrations of carrier transport and recombination.

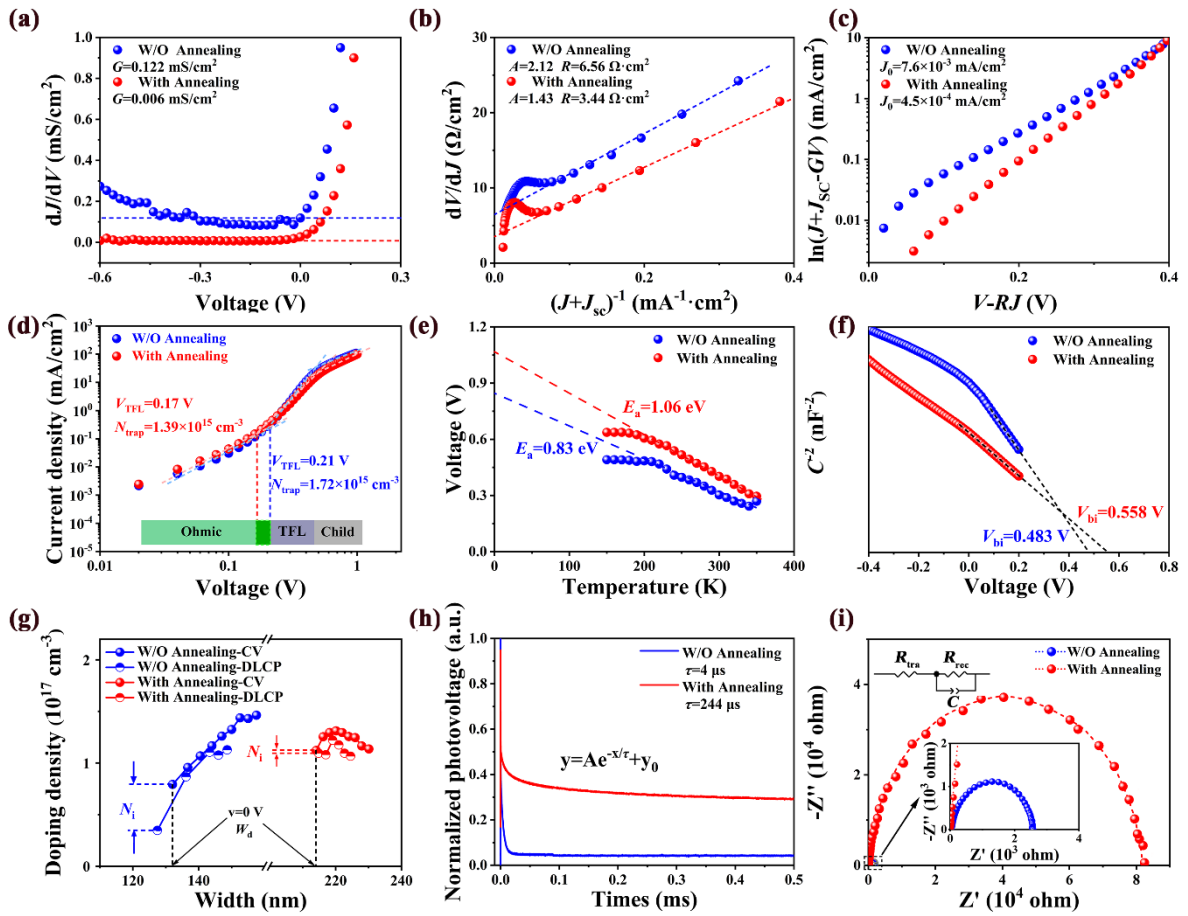

Figure 5. (a) Conductance G, (b) series resistance R and ideality factor A, (c) reverse saturation current density J_0 obtained from dark J-V curves of the W/O annealing and With annealing devices. (d) $V_{OC} - T$ measurements, (e) $1/C^2$–V plots, (f) C–V and DLCP profiles, (g) TPV decay curves, and (h) Nyquist plots of the W/O annealing and With annealing Sb_2Se_3/SnO_x devices.

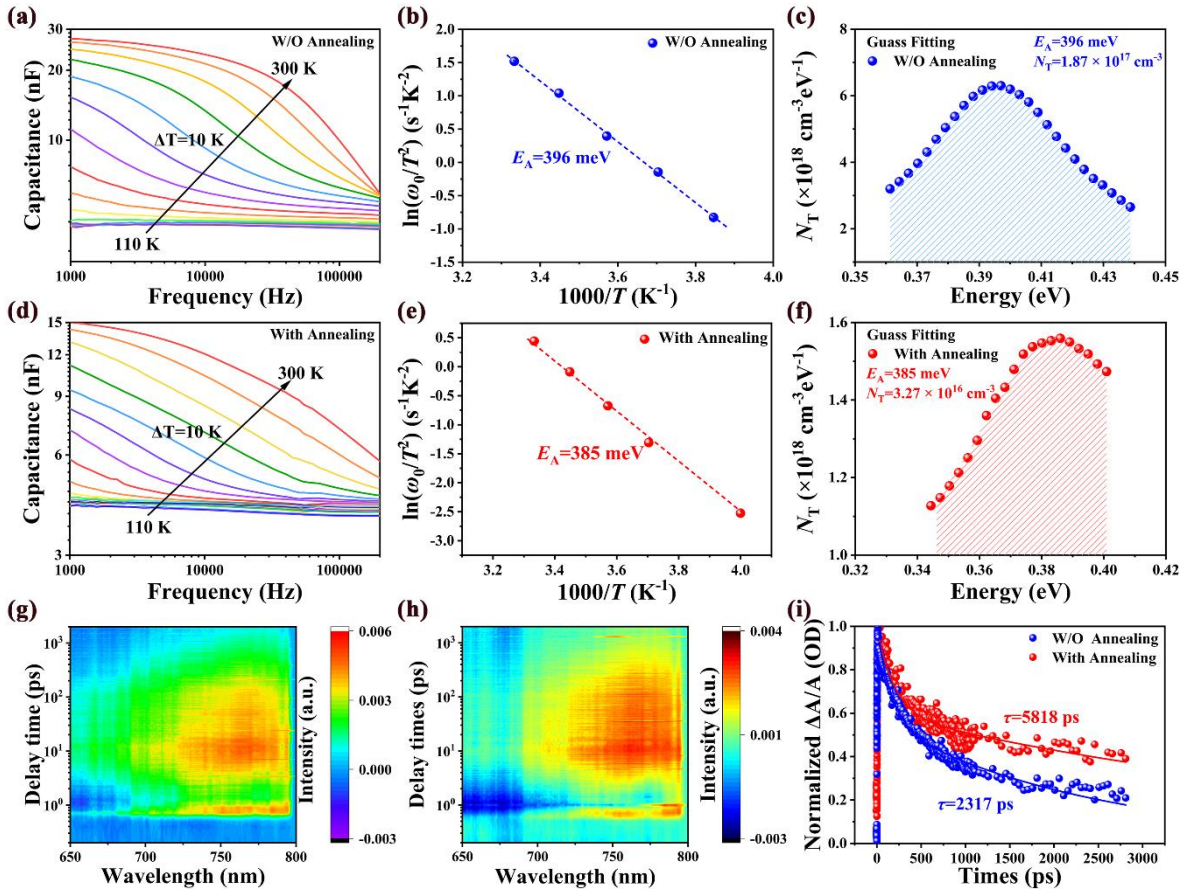

Figure 6. AS and TAS characterizations of the devices. (a, d) *C*−*f*−*T* spectra, (b, e) the Arrhenius plots for defect activation energy E_A calculation, and (c, f) the defect densities of the W/O annealing and With annealing Sb_2Se_3/SnO_x devices, respectively. 2D color mappings of the TA spectra of (g) W/O annealing and (h) With annealing Sb_2Se_3/SnO_x thin-film samples. (i) Transient kinetic traces of the decay of the PIA peak at 750 nm for both samples.

Table 1. Key photovoltaic parameters of the champion W/O annealing and With annealing Sb_2Se_3/SnO_x thin-film devices.

Devices	J_{SC} (mA/cm^2)	V_{OC} (V)	FF (%)	PCE (%)
W/O Annealing	23.22	0.370	53.99	4.64
With Annealing	29.34	0.407	61.96	7.39

Table 2. Electrical parameters derived from the heterojunction and interfaces of the W/O annealing and With annealing photovoltaic devices.

Devices	V_{TFL} (V)	N_{trap} (cm^{-3})	E_a (eV)	V_{bi} (V)	W_d (nm)	N_i (cm^{-3})	τ_{TPV} (μs)	R_{tra} (Ω/cm^2)
W/O Annealing	0.21	1.72×10^{15}	0.83	0.483	128	4.45×10^{16}	4	25.98
With Annealing	0.17	1.39×10^{15}	1.06	0.558	214	2.66×10^{15}	244	12.74

Table of contents: Actomic layer deposition processed SnO_x is introduced as electron tranport layer in Sb_2Se_3 thin-film solar cells. An additional post-annealing can remarkably enhance the photovoltaic performance, thanks to the optimized carrier dynamics under simultaneously improving the properties of SnO_x, Sb_2Se_3/SnO_x heterojunction and Sb_2Se_3 absorber layer. A stimulating efficiency of 7.39% represents the record value for Cd-free substrate structured Sb_2Se_3 solar cells.

Title: Electron Transport Layer Engineering Induced Carrier Dynamics Optimization for Efficient Cd-Free Sb_2Se_3 Thin-Film Solar Cells

ToC figure

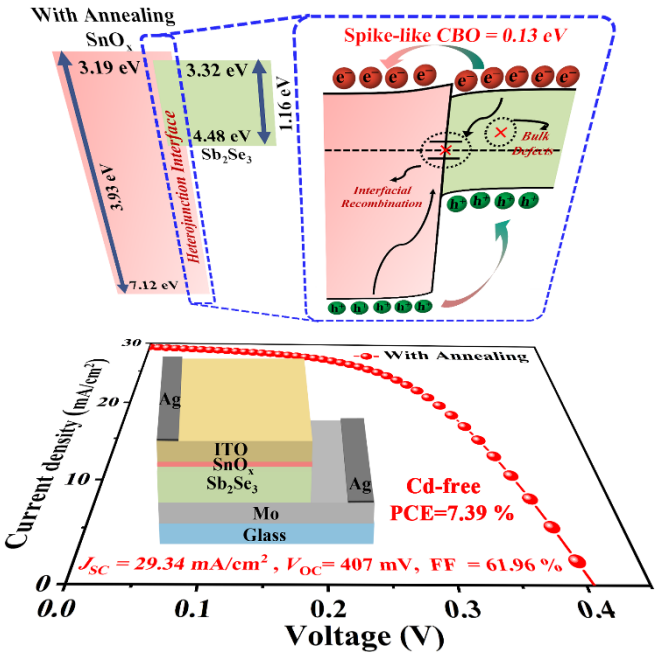

Supporting Information

Electron Transport Layer Engineering Induced Carrier Dynamics Optimization for Efficient Cd-Free Sb_2Se_3 Thin-Film Solar Cells

*Ping Luo, Tahir Imran, Dong-Lou Ren, Jun Zhao, Ke-Wen Wu, Yu-Jia Zeng, Zheng-Hua Su, Ping Fan, Xiang-Hua Zhang, Guang-Xing Liang, and Shuo Chen**

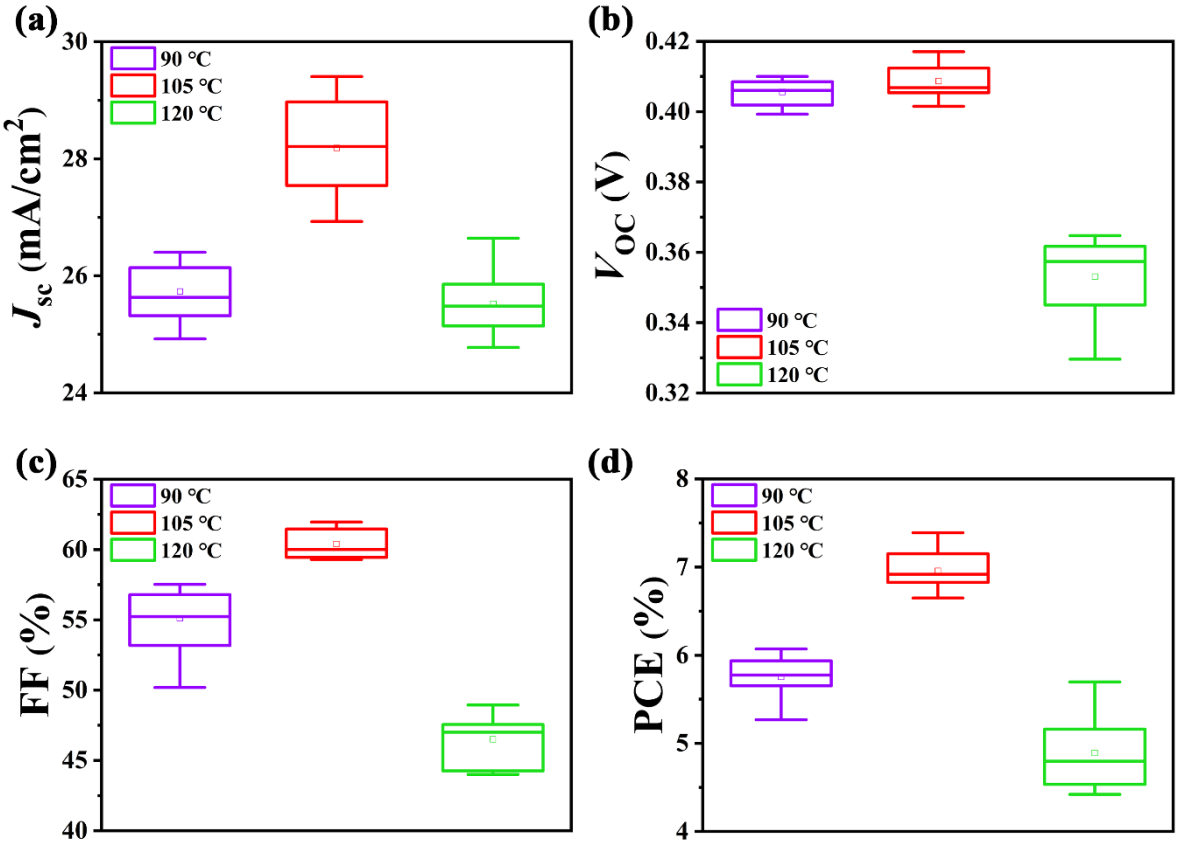

Figure S1. Statistical distributions of the key photovoltaic performance parameters of the Sb_2Se_3/SnO_x thin-film solar cells with different ALD preparation temperatures for SnO_x ETLs.

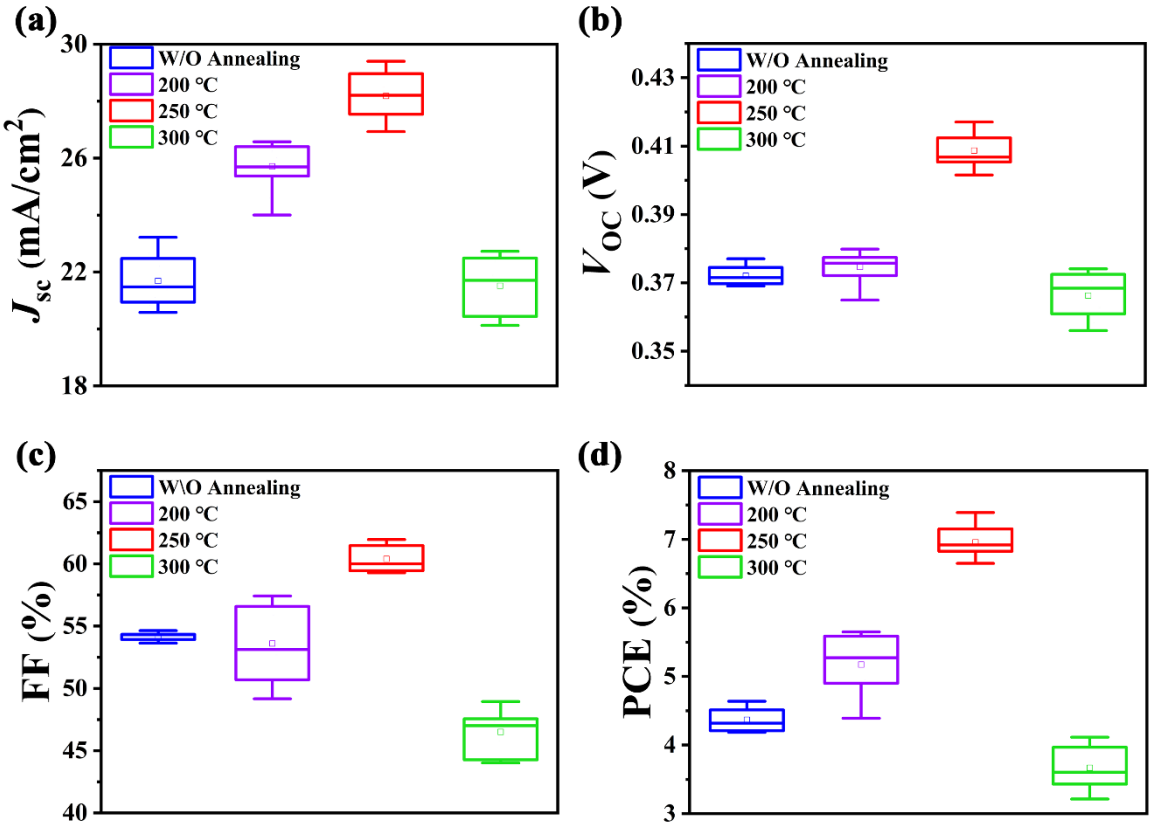

Figure S2. Statistical distributions of the key photovoltaic performance parameters of the Sb_2Se_3/SnO_x thin-film solar cells with different heterojunction post-annealing temperatures.

Table S1. A comparison of the key photovoltaic parameters to those of Cd-free Sb_2Se_3 solar cells.

Devices	V_{OC} (V)	J_{SC} (mA/cm^2)	FF (%)	PCE (%)	Publication year	Ref.
Mo/Sb_2Se_3/SnO_x/ITO/Ag	**0.407**	**29.34**	**61.96**	**7.39**		**This work**
FTO/TiO_2/Sb_2Se_3/P3HT/Au	0.44	31.98	48.77	6.88	2023	[1]
Mo/Sb_2Se_3/ZnO/PEI/AZO	0.344	20.67	34.42	2.41	2023	[2]
FTO/TiO_2/Sb_2Se_3/Spiro-OMeTAD/Au	0.451	29.85	59.7	8.03	2022	[3]
FTO/TiO_2/Sb_2Se_3/Spiro-OMeTAD/Au	0.38	27.2	58.56	6.06	2022	[4]
Mo/Sb_2Se_3-Cu/Sb_2Se_3-I/ITO/Ag	0.294	20	41	2.41	2022	[5]
FTO/TiO_2/Sb_2Se_3/Au	0.38	24.8	50	4.7	2022	[6]
FTO/SnO_2/Sb_2Se_3/P3HT/C	0.375	25.96	55.71	5.41	2022	[7]
Mo/Sb_2Se_3/ZnSnO/ITO/Ag	0.364	23.23	40.63	3.44	2022	[8]
ITO/SnO_2/TiO_2/Sb_2Se_3/Au	0.373	28.5	54.8	5.82	2022	[9]
ITO/TiO_2/Sb_2Se_3/Au	0.394	25.5	52.9	5.33	2021	[10]
FTO/TiO_2/Sb_2Se_3/Au	0.43	24.6	50	5.28	2021	[11]
Mo/Sb_2Se_3-Sn/Sb_2Se_3-I/ITO/Ag	0.28	22.45	34.51	2.17	2021	[12]
FTO/SnO_2/Sb_2Se_3/P3HT/C	0.354	23.63	56.81	4.76	2020	[13]
FTO/TiO_2/Sb_2Se_3/PbS-CQD/Au	0.386	32.6	60.6	7.62	2019	[14]
FTO/SnO_2-TiO_2/Sb_2Se_3/Au	0.335	25.3	47.2	4	2019	[15]
FTO/SnO_2/Sb_2Se_3/Au	0.297	23.58	46.4	3.25	2019	[16]
FTO/TiO_2/Sb_2Se_3/PCDTBT/Au	0.418	32.2	48.4	6.54	2018	[17]
FTO/SnO_2/Sb_2Se_3/Au	0.312	25.26	38.64	3.05	2017	[18]
FTO/TiO_2/Sb_2Se_3/Au	0.358	28.3	55.1	5.6	2017	[19]
FTO/ZnO/Sb_2Se_3/Au	0.391	26.2	57.8	5.93	2017	[20]
FTO/TiO_2/Sb_2Se_3/HTM/Au	0.305	22.3	47.2	3.21	2013	[21]

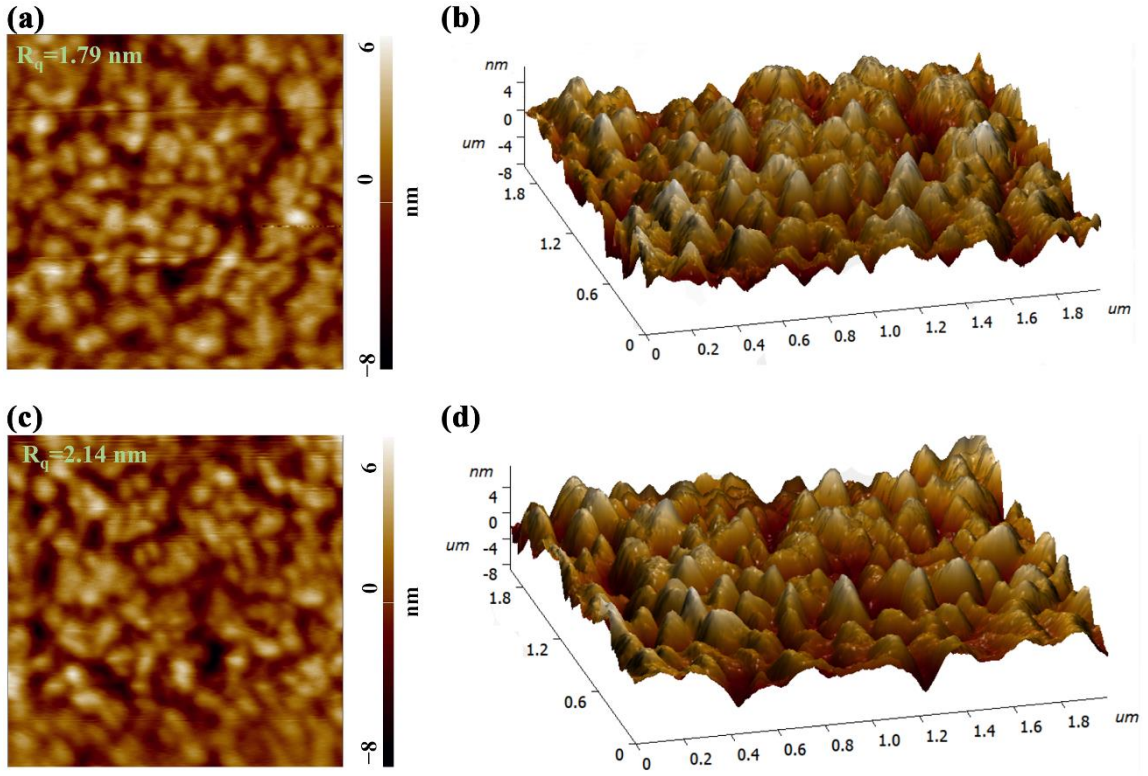

Figure S3. 2D/3D AFM micrographs of (a, b) W/O annealing, and (c, d) With annealing SnO_x thin films.

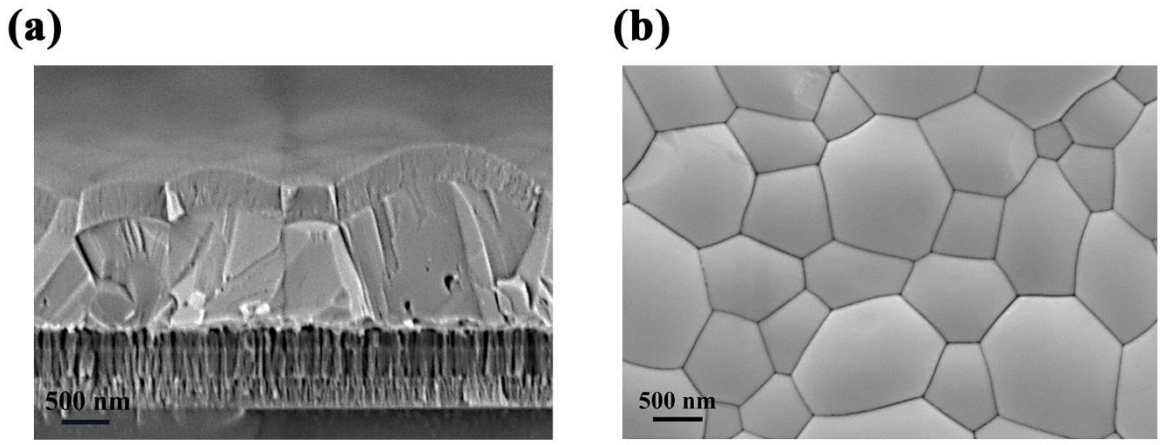

Figure S4. (a) Cross-sectional SEM image of the With annealing Sb_2Se_3/SnO_x thin-film solar cell, (b) SEM surface image of the Sb_2Se_3 thin film.

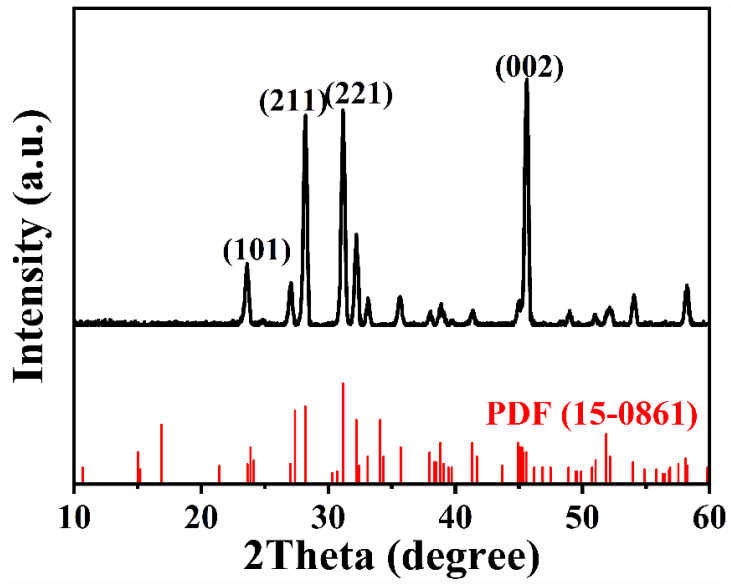

Figure S5. XRD pattern of the Sb_2Se_3 thin film.

Table S2. The percentage of area corresponding to each peak in XPS spectra of O 1s in the representative Sb_2Se_3/SnO_x thin films with and without post-annealing treatment.

	$O\text{-}Sn^{4+}$	$O\text{-}Sn^{2+}$	-OH	V_O
W/O Annealing	75.62	0.25	11.92	12.21
With Annealing	57.77	6.34	2.13	33.76

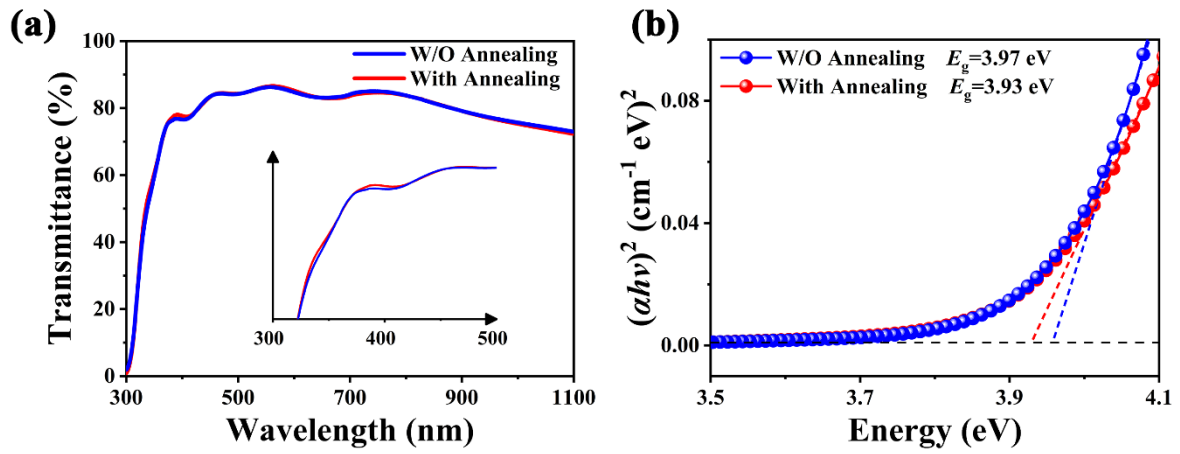

Figure S6. (a) Transmittance spectra of the W/O annealing and With annealing SnO_x thin films. (b) Plots of $(\alpha hv)^2$ versus hv, used to obtain the bandgap values.

Supplementary Note S1: Bandgap E_g calculation from transmittance spectra.

The transmittance spectra were treated to obtain the optical bandgap (E_g) values of the thin films using the following formula:[22]

$$\begin{cases} \alpha = \dfrac{ln\left(\frac{1}{T_1}\right)}{d} \\ \alpha hv = C\left(hv - E_g\right)^2 \end{cases} \quad \text{(S1)}$$

where α, d, and T_1 are absorption coefficient, thickness, and transmittance, respectively. C is a constant, h represents Planck's constant, v represents photon frequency in the latter Tauc formula. Therefore, the E_g value of the SnO_x thin film can be obtained by analyzing the linear extrapolated x-axis intercept of the plots of $(\alpha hv)^2$ versus Energy (Figure S6b).

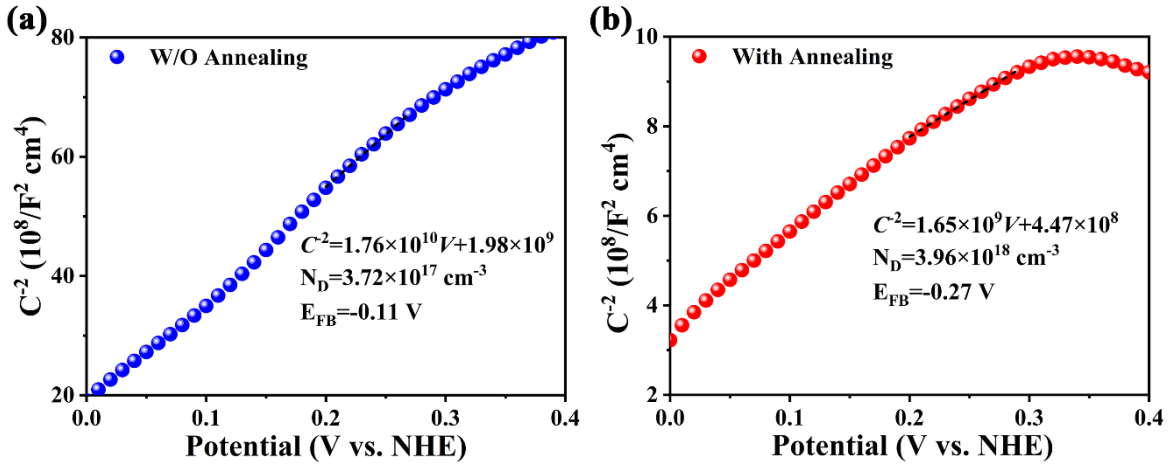

Figure S7. *M-S* plots of (a) W/O annealing and (b) With annealing SnO_x thin films.

Supplementary Note S2: E_{fb} and N_D calculations from M-S plots.

Mott-Schottky (*M-S*) measurements are applied by detecting the capacitance (C) formed at semiconductor-electrolyte contact as a function of the applied potential (V). Figure S7 demonstrates that $1/C^2$ is directly proportional to V within the presence of SCR, indicating a typical n-type behavior for both annealed and non-annealed SnO_x thin film samples. Moreover, the carrier density (N_D) and flat band potential (E_{fb}) can be determined utilizing the following equations: [22,23]

$$N_D = \left(\frac{2}{q\varepsilon\varepsilon_0}\right)\left[\frac{d\left(\frac{1}{C^2}\right)}{dV}\right]^{-1}$$
$$\left(\frac{1}{C^2} = \frac{2}{q\varepsilon\varepsilon_0 N_D}\left[(V - E_{fb}) - \frac{k_B T}{q}\right]\right. \quad \text{(S2)}$$

where q is the unit charge, ε is the relative dielectric constant, ε_0 is the vacuum permittivity, k_B is the Boltzmann constant, and T represents the temperature. Hence, the carrier density (N_D) and flat band potential (E_{fb}) can be determined by analyzing the slope and x-axis intercept of the corresponding linear region, respectively.

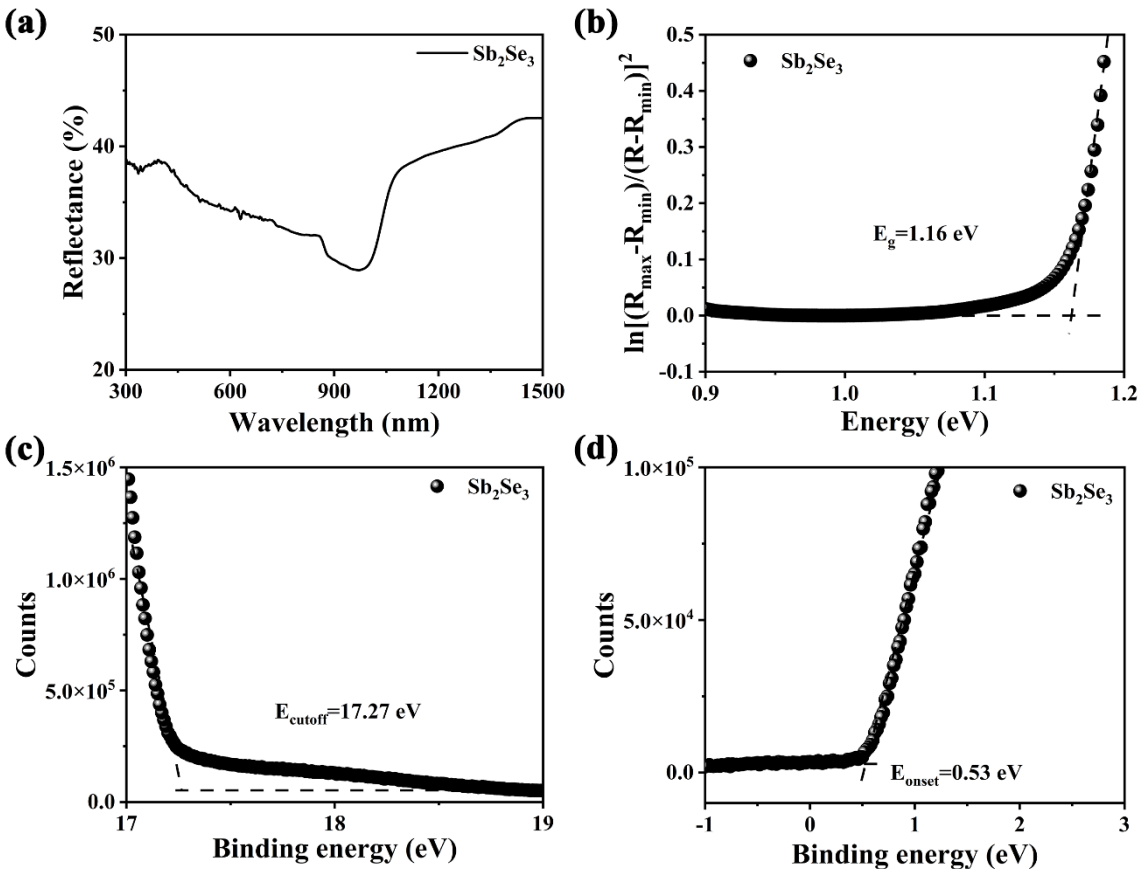

Figure S8. (a) Reflectance spectra of the Sb_2Se_3 thin film. (b) Plot of $(\alpha hv)^2$ versus hv. (c, d) UPS characterizations of the Sb_2Se_3 thin film, used to obtain (c) E_{cutoff} and (d) E_{onset} position.

Supplementary Note S3: Bandgap E_g calculation from reflectance spectrum.

Herein, the reflactance spectrum is applied to extract the E_g value of the Sb_2Se_3 thin films using the following formulas: [23,24]

$$\begin{cases} 2\alpha d = ln\left(\frac{R_{max}-R_{min}}{R-R_{min}}\right) \\ \alpha hv = C\left(hv - E_g\right)^2 \end{cases} \quad \text{(S3)}$$

where α is the absorption coefficient, d is thickness, the reflectance falls from R_{max} to R_{min} due to the intrinsic absorption of light. The latter is also a Tauc formula. E_g value can be determined by analyzing the linear extrapolated x-axis intercept of the plot of $\ln[(R_{max}-R_{min})/(R-R_{min})]^2$ versus Energy (Figure S8b).

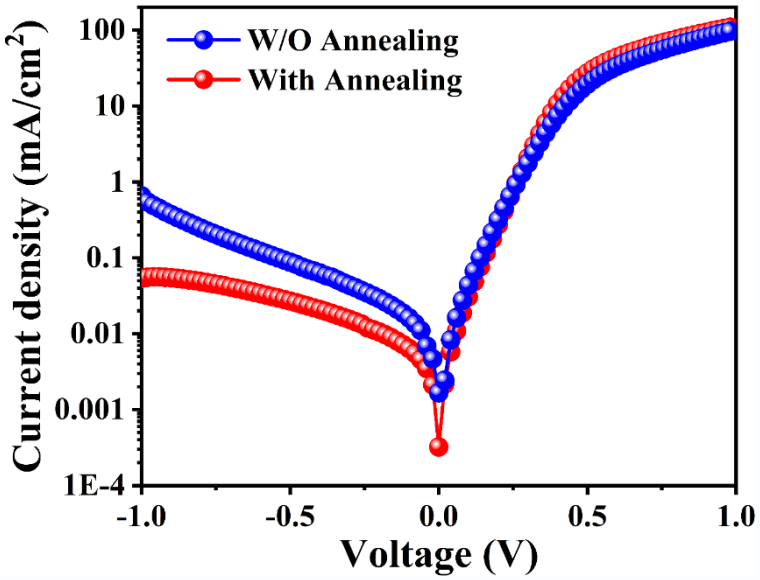

Figure S9. Dark *J-V* curves of the representative W/O annealing and With annealing devices.

Table S3. Fitted parameters for transient kinetic traces of the W/O annealing and With annealing samples. The average lifetime τ was calculated according to the equation: $\tau = (A_1\tau_1^2 + A_2\tau_2^2) / (A_1\tau_1 + A_2\tau_2)$.

Devices	A_1	τ_1 (ps)	A_2	τ_2 (ps)	τ (ps)
W/O Annealing	0.435	162	0.565	2428	2317
With Annealing	0.398	192	0.602	5938	5818

Table S4. A comparison of TAS measured carrier lifetime (τ) of Sb_2Se_3.

Samples	PCE (%)	τ (ps)	Method	Ref.
FTO/CdS/Sb_2Se_3	7.6%	1339	TAS	[25]
Glass/Sb_2Se_3	8.64%	5662	TAS	[26]
Glass/Sb_2Se_3	6.06%	4556	TAS	[4]
Glass/Sb_2Se_3	6.2%	4590	TAS	[27]
FTO/CdS/Sb_2Se_3	10.57%	6549	TAS	[28]
FTO/CdS/Sb_2Se_3	6.89%	6684	TAS	[29]
FTO/Sb_2Se_3/SnO_x	7.39%	5818	TAS	This work

Figure S10. Schematic diagram of the ALD pulse program for SnO_x ETL.

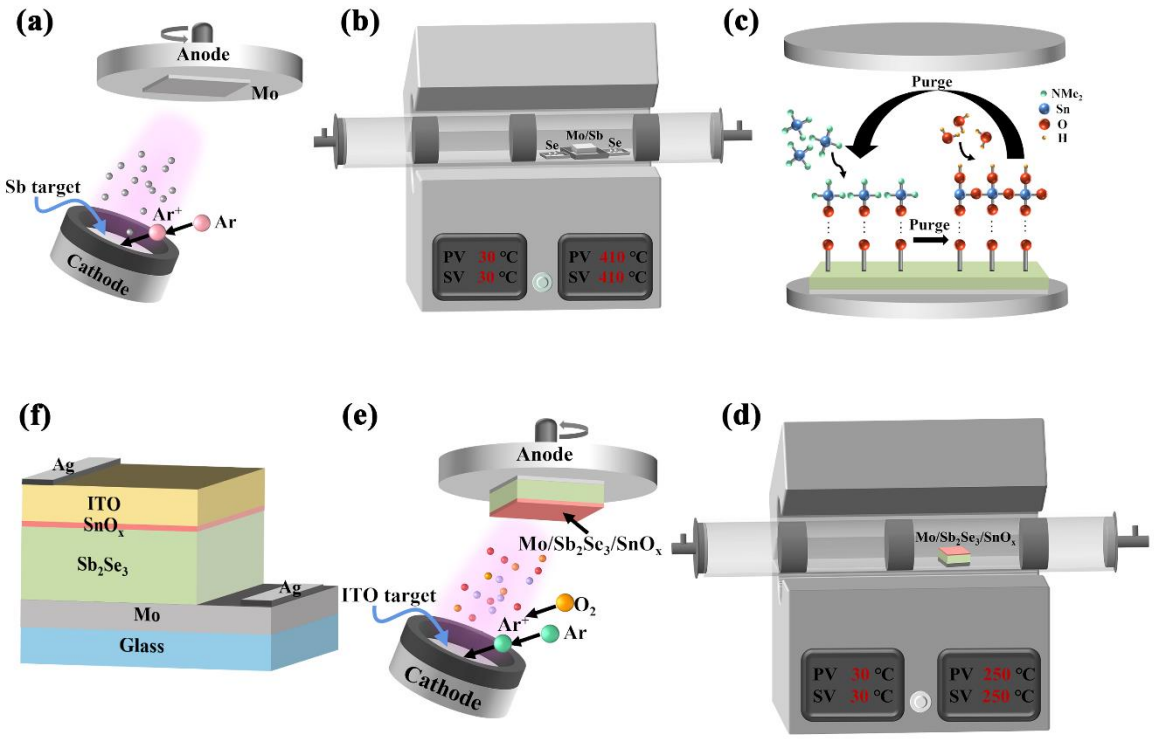

Figure S11. Schematic diagram of the preparation process of the Sb_2Se_3/SnO_x thin-film solar cell. (a) RF magnetron sputtering process for Sb precursor thin film. (b) Selenization heat treatment for Sb_2Se_3 thin film. (c) SnO_x ETL deposited via ALD method. (d) Heterojunction post-annealing treatment for Sb_2Se_3/SnO_x. (e) ITO window layer deposited by RF magnetron sputtering. (f) Schematic configuration of the Sb_2Se_3/SnO_x thin-film solar cell.

References

[1] C. H. Don, T. P. Shalvey, M. J. Smiles, L. Thomas, L. J. Phillips, T. D. C. Hobson, H. Finch, L. A. H. Jones, J. E. N. Swallow, N. Fleck, C. Markwell, P. K. Thakur, T. L. Lee, D. Biswas, L. Bowen, B. A. D. Williamson, D. O. Scanlon, V. R. Dhanak, K. Durose, T. D. Veal, J. D. Major, *Adv. Mater. Interfaces*, **2023**.

[2] D. Rovira, E. Ros, T. Tom, M. Jiménez, J. Miguel Asensi, C. Voz, J. López-Vidrier, J. Puigdollers, J. Bertomeu, E. Saucedo, *Int. J. Mol. Sci.*, **2023**.

[3] C. Liu, S. Wu, Y. Gao, Y. Feng, X. Wang, Y. Xie, J. Zheng, H. Zhu, Z. Li, R. E. I. Schropp, K. Shen, Y. Mai, *Adv. Funct. Mater.*, **2022**, 32, 2209601.

[4] Y. Wang, R. Tang, L. Huang, C. Qian, W. Lian, C. Zhu, T. Chen, *ACS Appl. Mater. Interfaces*, **2022**, 14, 33181-33190.

[5] D. Ren, C. Li, Z. Li, B. Zhu, B. Fu, J. Ji, S. Chen, G. Liang, H. Ma, X. Zhang, *J. Alloys*

Compd., **2023**, 960, 170753.

[6] M. Koltsov, R. Krautmann, A. Katerski, N. Maticiuc, M. Krunks, I. Oja Acik, N. Spalatu, *Faraday Discuss.*, **2022**, 239, 273-286.

[7] J. Zhou, D. Meng, T. Yang, X. Zhang, Z. Tang, Y. Cao, J. Ni, J. Zhang, Z. Hu, J. Pang, *Appl. Surf. Sci.*, **2022**, 591, 153169.

[8] Y. D. Luo, M. D. Chen, R. Tang, M. Azam, S. Chen, Z. H. Zheng, Z.-H. Su, P. Fan, H. L. Ma, G. X. Liang, X. H. Zhang, *Sol. Energy Mater. Sol. Cells*, **2022**, 240, 111721.

[9] W. Wang, L. Yao, J. Dong, L. Wu, Z. Cao, L. Hui, G. Chen, J. Luo, Y. Zhang, *Adv. Mater. Interfaces*, **2022**, 9, 2102464.

[10] W. Wang, Z. Cao, H. Wang, J. Luo, Y. Zhang, *J. Mater. Chem. A*, **2021**, 9, 26963-26975.

[11] N. Spalatu, R. Krautmann, A. Katerski, E. Karber, R. Josepson, J. Hiie, I. O. Acik, M. Krunks, *Sol. Energy Mater. Sol. Cells*, **2021**, 225, 111045.

[12] G. Liang, X. Chen, D. Ren, X. Jiang, R. Tang, Z. Zheng, Z. Su, P. Fan, X. Zhang, Y. Zhang, S. Chen, *J. Materiomics*, **2021**, 7, 1324-1334.

[13] J. Zhou, X. Zhang, H. Chen, Z. Tang, D. Meng, K. Chi, Y. Cai, G. Song, Y. Cao, Z. Hu, *Appl. Surf. Sci.*, **2020**, 534, 147632.

[14] K. Li, C. Chen, S. Lu, C. Wang, S. Wang, Y. Lu, J. Tang, *Adv. Mater.*, **2019**, 31, 1903914.

[15] X. Wang, H. Guo, C. Ma, X. Jia, Y. Li, N. Yuan, J. Ding, *Vacuum*, **2019**, 166, 201-205.

[16] Z. Chen, H. Guo, C. Ma, X. Wang, X. Jia, N. Yuan, J. Ding, *Sol. Energy*, **2019**, 187, 404-410.

[17] O. S. Hutter, L. J. Phillips, K. Durose, J. D. Major, *Sol. Energy Mater. Sol. Cells*, **2018**, 188, 177-181.

[18] S. Lu, Y. Zhao, C. Chen, Y. Zhou, D. Li, K. Li, W. Chen, X. Wen, C. Wang, R. Kondrotas, N. Lowe, J. Tang, *Adv. Electron. Mater.*, **2018**, 4, 1700329.

[19] C. Chen, Y. Zhao, S. Lu, K. Li, Y. Li, B. Yang, W. Chen, L. Wang, D. Li, H. Deng, F. Yi, J. Tang, *Adv. Energy Mater.*, **2017**, 7, 1700866.

[20] L. Wang, D. B. Li, K. Li, C. Chen, H. X. Deng, L. Gao, Y. Zhao, F. Jiang, L. Li, F. Huang, Y. He, H. Song, G. Niu, J. Tang, *Nat. Energy*, **2017**, 2, 17046.

[21] Y. C. Choi, T. N. Mandal, W. S. Yang, Y. H. Lee, S. H. Im, J. H. Noh, S. I. Seok, *Angew. Chem. Int. Ed.*, **2014**, 53, 1329-1333.

[22] S. Chen, T. Liu, M. Chen, M. Ishaq, R. Tang, Z. Zheng, Z. Su, X. Li, X. Qiao, P. Fan, G. Liang, *Nano Energy*, **2022**, 99, 107417.

[23] G. Liang, Z. Li, M. Ishaq, Z. Zheng, Z. Su, H. Ma, X. Zhang, P. Fan, S. Chen, *Adv. Energy Mater.*, **2023**, 13, 2300215.

[24] G. Liang, T. Liu, M. Ishaq, Z. Chen, R. Tang, Z. Zheng, Z. Su, P. Fan, X. Zhang, S. Chen, *Chem. Eng. J.*, **2022**, 431, 133359.

[25] X. Wen, C. Chen, S. Lu, K. Li, R. Kondrotas, Y. Zhao, W. Chen, L. Gao, C. Wang, J. Zhang, G. Niu, J. Tang, *Nat. Commun.*, **2018**, 9, 2179.

[26] R. Tang, S. Chen, Z.-H. Zheng, Z.-H. Su, J.-T. Luo, P. Fan, X.-H. Zhang, J. Tang, G.-X. Liang, *Adv. Mater.*, **2022**, 34, 2109078.

[27] R. Cao, H. Cai, W. Lian, R. Tang, Y. Xiang, Y. Wang, T. Chen, *J. Mater. Chem. A*, **2022**, 10, 20482-20488.

[28] Y. Zhao, S. Wang, C. Li, B. Che, X. Chen, H. Chen, R. Tang, X. Wang, G. Chen, T. Wang, J. Gong, T. Chen, X. Xiao, J. Li, *Energy Environ. Sci.*, **2022**, 15, 5118-5128.

[29] H. Cai, R. Cao, J. Gao, C. Qian, B. Che, R. Tang, C. Zhu, T. Chen, *Adv. Funct. Mater.*, **2022**, 32, 2208243.